



# High Dense Gas Fraction in a Gas-rich Star-forming Galaxy at $z = 1.2^*$

Avani Gowardhan<sup>1</sup>, Dominik A. Riechers<sup>1</sup>, Emanuele Daddi<sup>2</sup>, Riccardo Pavesi<sup>1</sup>, Helmut Dannerbauer<sup>3,4</sup>, and Chris Carilli<sup>5</sup><sup>1</sup>Department of Astronomy, Cornell University, Ithaca, NY 14853, USA; [ag2255@cornell.edu](mailto:ag2255@cornell.edu)<sup>2</sup>CEA Saclay, Laboratoire AIM-CNRS-Université Paris Diderot, Ifu/SAP, Orme des Merisiers, F-91191 Gif-sur-Yvette, France<sup>3</sup>Instituto de Astrofísica de Canarias (IAC), E-38205 La Laguna, Tenerife, Spain<sup>4</sup>Universidad de La Laguna, Dpto. Astrofísica, E-38206 La Laguna, Tenerife, Spain<sup>5</sup>National Radio Astronomy Observatory, P.O. Box O, Socorro, NM 87801, USA

Received 2016 October 6; revised 2017 March 6; accepted 2017 March 7; published 2017 April 3

## Abstract

We report observations of dense molecular gas in the star-forming galaxy EGS 13004291 ( $z = 1.197$ ) using the Plateau de Bure Interferometer. We tentatively detect HCN and HNC  $J = 2 \rightarrow 1$  emission when stacked together at  $4\sigma$  significance, yielding line luminosities of  $L'_{\text{HCN}(J=2\rightarrow 1)} = (9 \pm 3) \times 10^9 \text{ K km s}^{-1} \text{ pc}^2$  and  $L'_{\text{HNC}(J=2\rightarrow 1)} = (5 \pm 2) \times 10^9 \text{ K km s}^{-1} \text{ pc}^2$ , respectively. We also set  $3\sigma$  upper limits of  $<7\text{--}8 \times 10^9 \text{ K km s}^{-1} \text{ pc}^2$  on the  $\text{HCO}^+(J = 2 \rightarrow 1)$ ,  $\text{H}_2\text{O}(3_{13} \rightarrow 2_{20})$ , and  $\text{HC}_3\text{N}(J = 20 \rightarrow 19)$  line luminosities. We serendipitously detect CO emission from two sources at  $z \sim 1.8$  and  $z \sim 3.2$  in the same field of view. We also detect  $\text{CO}(J = 2 \rightarrow 1)$  emission in EGS 13004291, showing that the excitation in the previously detected  $\text{CO}(J = 3 \rightarrow 2)$  line is subthermal ( $r_{32} = 0.65 \pm 0.15$ ). We find a line luminosity ratio of  $L'_{\text{HCN}}/L'_{\text{CO}} = 0.17 \pm 0.07$ , as an indicator of the dense gas fraction. This is consistent with the median ratio observed in  $z > 1$  galaxies ( $L'_{\text{HCN}}/L'_{\text{CO}} = 0.16 \pm 0.07$ ) and nearby ULIRGs ( $L'_{\text{HCN}}/L'_{\text{CO}} = 0.13 \pm 0.03$ ), but higher than that in local spirals ( $L'_{\text{HCN}}/L'_{\text{CO}} = 0.04 \pm 0.02$ ). Although EGS 13004291 lies significantly above the galaxy main sequence at  $z \sim 1$ , we do not find an elevated star formation efficiency (traced by  $L_{\text{FIR}}/L'_{\text{CO}}$ ) as in local starbursts, but a value consistent with main-sequence galaxies. The enhanced dense gas fraction, the subthermal gas excitation, and the lower than expected star formation efficiency of the dense molecular gas in EGS 13004291 suggest that different star formation properties may prevail in high- $z$  starbursts. Thus, using  $L_{\text{FIR}}/L'_{\text{CO}}$  as a simple recipe to measure the star formation efficiency may be insufficient to describe the underlying mechanisms in dense star-forming environments inside the large gas reservoirs.

*Key words:* galaxies: evolution – galaxies: high-redshift – galaxies: starburst – galaxies: star formation – ISM: molecules

## 1. Introduction

Over the past decade, there has been a surge in the number of galaxies at the peak epoch of star formation ( $z \sim 1\text{--}3$ ) in which molecular gas, the fuel for star formation, has been detected (see Carilli & Walter 2013 for a review). This includes a sizable sample of “normal” star-forming galaxies (SFGs; Daddi et al. 2008, 2010a; Tacconi et al. 2010, 2013); most of these fall on a tight relation between stellar mass ( $M_*$ ) and star formation rate ( $\text{SFR} \sim M_*^p$ ,  $p = 0.6\text{--}0.9$ ), the so-called star-forming “main sequence” (MS; Daddi et al. 2007; Elbaz et al. 2007; Noeske et al. 2007; Rodighiero et al. 2011; Wuyts et al. 2011; Whitaker et al. 2012). The specific star formation rate ( $\text{sSFR} = \text{SFR}/M_*$ ) remains roughly constant along the MS at each epoch but increases with redshift, consistent with the overall increase in the cosmic star formation rate density (e.g., Karim et al. 2011; Whitaker et al. 2012; Speagle et al. 2014; Lee et al. 2015). The existence of the galaxy MS shows that the bulk of cosmic star formation at high redshift proceeds in a quasi-steady state, over long timescales ( $\sim 1$  Gyr) and large spatial scales, while episodes of intense merger-induced starburst activity play a smaller role. Consequently, two main modes of star formation have been proposed for the high- $z$  SFG population: a quiescent star formation mode that dominates in MS galaxies, and an enhanced “starburst” mode of merger-driven star formation

commonly seen in outliers lying above the MS (Daddi et al. 2010b; Genzel et al. 2010; Rodighiero et al. 2011).

MS galaxies at  $z > 1$  have star formation rates that are 10–100 times higher than SFRs observed in normal galaxies in the local universe. A significant fraction of extreme high- $z$  galaxies such as submillimeter galaxies (SMGs) or merging Ultra-Luminous infrared galaxies (ULIRGs) are inconsistent with the MS (see Blain et al. 2002; Casey et al. 2014, for reviews) and display enhanced star formation efficiencies ( $\text{SFE}_{\text{mol}} = \text{SFR}/M_{\text{gas}}$ ) and short gas depletion timescales ( $\tau_{\text{depl}} = 1/\text{SFE}_{\text{mol}}$ ). However, it is yet unclear what fraction of the enhanced star formation rate in high- $z$  SFGs is driven by their high gas masses, as opposed to an increase in their SFE, and whether this fraction differs between SFGs lying on or above the galaxy MS (Daddi et al. 2015; Scoville et al. 2015; Silverman et al. 2015). While recent studies for above-MS galaxies at  $z \sim 1.6$  have found a higher  $L_{\text{FIR}}/L'_{\text{CO}}$ , that is, a higher SFE relative to MS galaxies, in seven outliers above the MS (Silverman et al. 2015), existing work is far from conclusive. Alternative theories suggest a single unified mode of intense star formation in all high- $z$  SFGs, driven by compression and turbulence in the interstellar medium (ISM), with constant replenishment of cold gas from the cosmic web (Bouché et al. 2010; Lilly et al. 2013). In this framework, all high- $z$  SFGs, including both MS and above-MS galaxies, have a near-constant gas depletion timescale (e.g., Scoville et al. 2015). Such a mode would be fundamentally different from that seen in IR-luminous starburst galaxies, which boast

\* Based on observations carried out under project ID U030 with the IRAM NOEMA Interferometer. IRAM is supported by INSU/CNRS (France), MPG (Germany), and IGN (Spain).

concentrated and short-lived star formation activity, or that in local spiral galaxies, where star formation primarily takes place in clumps of giant molecular clouds (GMCs), distributed throughout the diffuse molecular gas. As the molecular gas is strongly coupled to the star formation, we need to better characterize its properties in galaxies lying on and above the MS to identify the prevalent mode of star formation in high- $z$  SFGs.

The Kennicutt–Schmidt (KS) relation (Schmidt 1959; Kennicutt 1998) relates the local average gas density to the local SFR, typically traced using the FIR luminosity  $L_{\text{FIR}}$ . It also explains the observed correlation  $L_{\text{FIR}} \propto L'_{\text{CO}}{}^{1.5}$  (e.g., Sanders & Mirabel 1996; Kewley et al. 2002), where CO is typically used to trace molecular gas. However, ground-state CO transitions ( $n_{\text{crit}} \sim 10^3 \text{ cm}^{-3}$ ) trace both the dense and diffuse molecular gas due to their low critical density, while only the cold, dense component is immediately available for star formation.

Most of the star formation in the Milky Way and the local universe takes place in the dense cores of GMCs ( $n_{\text{H}_2} \sim 10^5 \text{ cm}^{-3}$ ), which are better traced by dense gas tracers such as HCN,  $\text{HCO}^+$ , and HNC ( $n_{\text{crit}} \sim 10^5 \text{ cm}^{-3}$ ) than by CO. There exists a strong linear correlation between  $L_{\text{FIR}}$  and  $L'_{\text{HCN}}$  (Gao & Solomon 2004b). This  $L_{\text{FIR}}-L'_{\text{HCN}}$  relation holds over seven orders of magnitude, ranging from GMCs in the Milky Way to high- $z$  galaxies (Gao & Solomon 2004b; Wu et al. 2005; Gao et al. 2007; Wu et al. 2010). This is a much tighter relation than the  $L_{\text{FIR}}-L'_{\text{CO}}$  relation, which also shows a change in slope depending on the sample selection (Sanders & Mirabel 1996; Solomon et al. 1997; Gao & Solomon 2004b). While such a relationship is shown by both HCN and  $\text{HCO}^+$  (Graciá-Carpio et al. 2006; Riechers et al. 2006a; Papadopoulos 2007; García-Burillo et al. 2012),  $\text{HCO}^+$  is more sensitive to ionization conditions and typically shows weaker emission than HCN. On the other hand, the HCN abundance can be enhanced by the presence of an active galactic nucleus (AGN) or mechanically driven shocks or outflows, contributing to nonlinearity in the  $L'_{\text{HCN}}-L_{\text{FIR}}$  relation for more FIR-luminous sources (García-Burillo et al. 2012; Martín et al. 2015; Privon et al. 2015; Izumi et al. 2016). Together, the relative intensities of dense gas tracers, HCN, HNC, and  $\text{HCO}^+(J=2 \rightarrow 1)$  allow us to probe the gas temperature and ionization (Costagliola et al. 2011). In addition, the line luminosity ratio  $L'_{\text{HCN}}/L'_{\text{CO}}$  is an indicator of the dense gas fraction  $f_{\text{dense}}$  and represents the *actively star-forming* fraction of molecular gas. As  $L'_{\text{HCN}}/L'_{\text{CO}}$ ,  $L_{\text{FIR}}/L'_{\text{HCN}}$ , and  $L_{\text{FIR}}/L'_{\text{CO}}$  vary significantly between different star formation environments, these are critical tools for identifying the dominant mode of star formation in high- $z$  SFGs, and they provide significantly more powerful constraints on the global star formation mechanisms than  $L_{\text{FIR}}/L'_{\text{CO}}$  alone.

However, studies of the dense molecular gas as traced by HCN require high observing sensitivity and thus have been mostly limited to the nearby universe. There are only three solid and three tentative detections at high redshift, including lensed systems, (U)LIRGs, and SMGs (e.g., Gao et al. 2007; Riechers et al. 2007, and references therein); there are no such observations for normal, unlensed SFGs at high redshift.

In this paper, we present for the first time observations of the dense, actively star-forming gas in a massive star-forming galaxy, EGS 13004291, at high redshift ( $z = 1.197$ ). EGS 13004291 is the most CO-luminous source in the currently known sample of high- $z$  SFGs (Daddi et al. 2010b; Tacconi

et al. 2013) and is therefore the best candidate for this initial study of the dense gas fraction in high- $z$  SFGs.

The paper is organized as follows. In Section 2 and Section 3, we present the observations and results. In Section 4, we discuss our analysis, including line stacking and spectral energy distribution (SED) fitting, as well as the serendipitous detection of two sources. In Section 5 and Section 6, we discuss our results and conclusions. We use a  $\Lambda$ CDM cosmology, with  $H_0 = 71 \text{ km s}^{-1} \text{ Mpc}^{-1}$ ,  $\Omega_{\text{M}} = 0.27$ , and  $\Omega_{\Lambda} = 0.73$  (Spergel et al. 2007).

## 2. Observations

### 2.1. IRAM Observations

We observed the primary target EGS 13004291 (J2000 R.A.:  $14^{\text{h}}19^{\text{m}}15^{\text{s}}.0$ , decl.:  $+52^{\text{d}}49^{\text{m}}30^{\text{s}}$ ,  $z = 1.197$ ) with the IRAM Plateau de Bure Interferometer (PdBI) with five antennas in the compact D configuration during five tracks in 2010 May–June, with a total on-source time of 11.5 hr. Weather conditions were average or better for 3 mm observations, with a precipitable water vapor of 6–7 mm for all tracks. The absolute flux scale was calibrated either on 3C273, MWC349, or 3C345. The source J1418+546 was used as a phase and bandpass calibrator. The WideX correlator (bandwidth  $\sim 3.6$  GHz) was used to observe multiple molecular lines simultaneously. Observations were carried out in dual polarization mode, using a tuning frequency of 81.95 GHz and a binned spectral resolution of 3.9 MHz ( $\sim 14.2 \text{ km s}^{-1}$  at 81.95 GHz), covering the frequency range  $\nu_{\text{obs}} = 80.6833\text{--}83.4366$  GHz. This covered the redshifted HCN ( $J = 2 \rightarrow 1$ ), HNC ( $J = 2 \rightarrow 1$ ),  $\text{HCO}^+(J = 2 \rightarrow 1)$ ,  $\text{HC}_3\text{N}$  ( $J = 20 \rightarrow 19$ ), and  $\text{H}_2\text{O}(3_{13} \rightarrow 2_{20})$  lines at  $z = 1.197$  (see Table 1 for rest frequencies).

In a second tuning, we observed the CO ( $J = 2 \rightarrow 1$ ) line ( $\nu_{\text{rest}} = 230.538$  GHz) in 2010 May for 0.6 hr on source, under excellent weather conditions for 3 mm observing, using six antennas and recording data from both the narrow-band (bandwidth  $\sim 1.0$  GHz) and the WideX correlator. We used a tuning frequency of 104.933 GHz and binned spectral resolutions of 10 and 2 MHz, corresponding to  $28 \text{ km s}^{-1}$  and  $5.6 \text{ km s}^{-1}$  at 105 GHz, respectively. The data were taken in dual polarization mode, using MWC349 as the absolute flux calibrator.

All observations were calibrated using the IRAM PdBI data reduction pipeline in CLIC (Continuum and Line Interferometer Calibration),<sup>6</sup> with subsequent additional flagging by hand. The absolute flux scale was calibrated to better than 20% for both CO and HCN observations.

The reduced visibility cube for the dense gas tracers was imaged using UV\_MAP, with natural weighting and a pixel size of  $0''.5 \times 0''.5$ , and cleaned using the task CLEAN with the Hogbom algorithm, after binning over a large velocity width, 40 channels at our spectral resolution (corresponding to  $\sim 590 \text{ km s}^{-1}$ ). The resulting cleaned image has an rms noise of  $0.15 \text{ mJy beam}^{-1}$  and a synthesized beam size of  $6''.0 \times 5''.0$ , with a position angle (PA) of  $-72^\circ.3$ . The antenna half-power beam width is  $61''$ , and primary beam correction was applied using the task PRIMARY.

The task UV\_MAP was used to image the calibrated visibility CO ( $J = 2 \rightarrow 1$ ) cube, using natural weighting and a pixel size of  $0''.5 \times 0''.5$ ; the clean map was made using the task CLEAN,

<sup>6</sup> <http://www.iram.fr/IRAMFR/GILDAS>

**Table 1**  
Observed Line Properties for EGS 13004291

| Transition   | $\nu_{\text{rest}}$<br>(GHz) | $\nu_{\text{obs}}$<br>(GHz) | $I$<br>(Jy km s <sup>-1</sup> ) | $L'$<br>(10 <sup>10</sup> K km s <sup>-1</sup> pc <sup>2</sup> ) | References <sup>a</sup> |
|--|------------------------------|-----------------------------|---------------------------------|--|-------------------------|
| CO( $J = 2 \rightarrow 1$ )                                  | 230.5379                     | 104.961                     | $3.09 \pm 0.27$                 | $6.0 \pm 0.5$  | (1)                     |
| CO( $J = 3 \rightarrow 2$ )                                  | 345.7959                     | 157.394                     | $4.6 \pm 0.1$                   | 3.9  | (2)                     |
| HCN( $J = 2 \rightarrow 1$ )                                 | 177.2612                     | 80.704                      | $0.28 \pm 0.09$                 | $0.9 \pm 0.3$  | (1)                     |
| HNC( $J = 2 \rightarrow 1$ )                                 | 181.3248                     | 82.555                      | $0.17 \pm 0.07$                 | $0.5 \pm 0.2$  | (1)                     |
| HC <sub>3</sub> N( $J = 20 \rightarrow 19$ ) <sup>b</sup>    | 181.9449                     | 82.837                      | <0.21                           | <0.65  | (1)                     |
| HCO <sup>+</sup> ( $J = 2 \rightarrow 1$ ) <sup>b</sup>      | 178.3750                     | 81.212                      | <0.23                           | <0.76  | (1)                     |
| H <sub>2</sub> O( $3_{13} \rightarrow 2_{20}$ ) <sup>b</sup> | 183.3101                     | 83.459                      | <0.22                           | <0.66  | (1)                     |

**Notes.**

<sup>a</sup> (1) This work. (2) Tacconi et al. (2013).

<sup>b</sup>  $3\sigma$  upper limits obtained as described in Section 3.2.

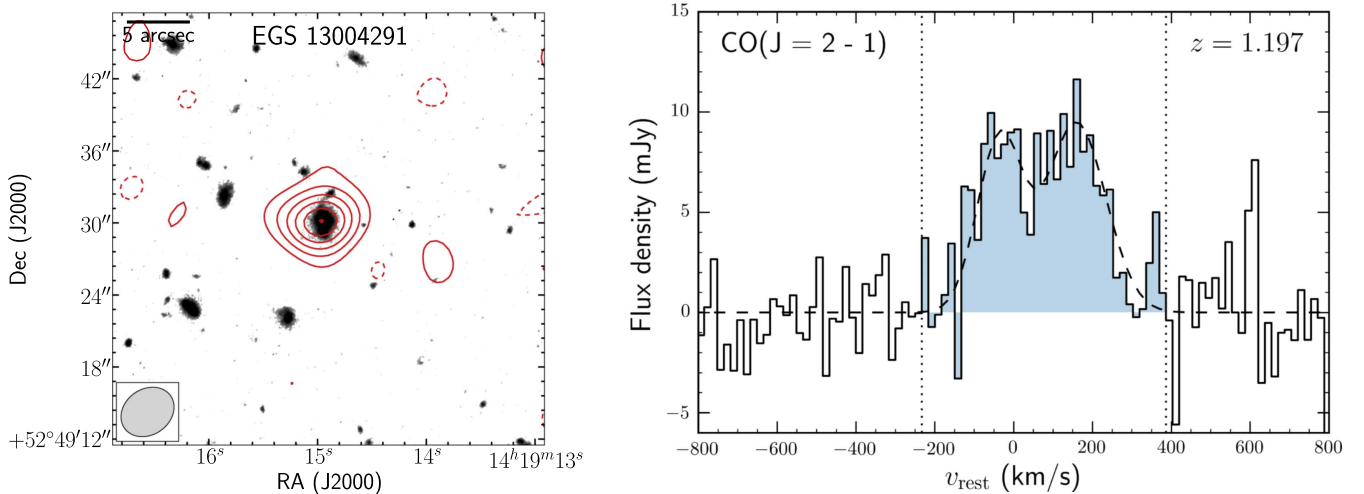


**Figure 1.** Left: CO( $J = 2 \rightarrow 1$ ) moment-0 map for EGS 13004291, made by collapsing the cleaned cube along the frequency axis over the velocity range  $-230$  to  $386$  km s<sup>-1</sup> (shown as dotted lines in the spectrum). The source is detected at  $\sim 12\sigma$  significance, where  $1\sigma \sim 0.3$  Jy km s<sup>-1</sup>. The relative contours at  $\pm 2, 4, 6, 8, 10, 12\sigma$  are shown, overlaid on the 3D-HST  $H$ -band image (Brammer et al. 2012; Skelton et al. 2014). The synthesized beam has a size of  $\sim 4''.7 \times 3''.8$  and is indicated in the bottom left corner. Right: spectrum extracted from the cleaned cube at the central pixel, with a velocity resolution of  $\sim 17$  km s<sup>-1</sup>. The dashed line shows a two-component Gaussian fit to the data.

using the Hogbom algorithm in MAPPING with natural weighting. For the CO observations, the cleaned image has an rms noise of  $2.3$  mJy beam<sup>-1</sup> in each channel (width  $\sim 17$  km s<sup>-1</sup>) and a synthesized beam size of  $4''.7 \times 3''.8$ , with a position angle (PA) of  $-66.5^\circ$ . The antenna half-power beam width is  $49''$ .

## 2.2. Archival Data

EGS 13004291 is located in the Extended Groth Strip, and as such has rich multiwavelength coverage from the All-Wavelength Extended Groth Strip International Survey (AEGIS). This includes observations with *Chandra* (2–10 keV; Laird et al. 2009; Nandra et al. 2015), *Galaxy Evolution Explorer* (GALEX), *Hubble Space Telescope* (HST) as part of the 3D-HST survey (Brammer et al. 2012; Skelton et al. 2014), *Spitzer* IRAC (Barmby et al. 2008), and *Herschel* PACS/SPIRE observations, as part of the NEWFIRM Medium-band Survey (NMBS; Davis et al. 2007; Whitaker et al. 2011).

To enable a comparison of our source properties against different galaxy populations, we have compiled a large sample of sources from the literature, both local and at high redshift, with extant observations in the FIR, CO (Weiß et al. 2003, 2007; Greve et al. 2005; Riechers et al. 2006b, 2009b, 2011a;

Danielson et al. 2011; Thomson et al. 2012), and HCN (Solomon et al. 2003; Vanden Bout et al. 2004; Gao & Solomon 2004a; Isaak et al. 2004; Carilli et al. 2005; Wagg et al. 2005; Evans et al. 2006; Greve et al. 2006; Gao et al. 2007; Graciá-Carpio et al. 2008; Krips et al. 2010; Riechers et al. 2010a; García-Burillo et al. 2012). All obtained luminosities have been adjusted to the cosmology used here; HCN detections with single-dish telescopes pointed at galactic nuclear regions have been treated as lower limits on the HCN luminosity where appropriate. We exclude sources with upper or lower limits on luminosities from all relevant calculations and sample averages, and we only use sources that have solid detections.

## 3. Results

### 3.1. CO( $J = 2 \rightarrow 1$ )

We successfully detect the CO( $J = 2 \rightarrow 1$ ) line in EGS 13004291 at a redshift of  $z = 1.197$ . We find that the emission is spatially unresolved, consistent with what is expected based on the previously measured CO( $J = 3 \rightarrow 2$ ) size (Tacconi et al. 2013;  $r_{1/2} \sim 0''.5$ ). We therefore extract the spectral profile (Figure 1) from the peak pixel (J2000 R.A.:  $14^{\text{h}}19^{\text{m}}14^{\text{s}}.97$ ; decl.:  $+52^{\circ}49^{\text{m}}29^{\text{s}}.73$ ). The spectrum is fit with a 1D Gaussian to estimate the line peak, velocity width, and central redshift; we

find the line center at  $\nu_{\text{obs}} = 104.961 \pm 0.005$  GHz corresponding to a redshift of  $z = 1.1964 \pm 0.0001$ . The moment-0 map (Figure 1) is created by collapsing the spectral cube along the frequency axis for the FWZI velocity width derived from this best fit ( $\Delta\nu_{\text{FWZI}} \sim 620$  km s<sup>-1</sup>). Finally, the area under the spectral line fit is used to obtain an integrated line flux of  $I_{\text{CO}} = 3.09 \pm 0.27$  Jy km s<sup>-1</sup>; this is consistent with the value derived from the peak of the moment-0 map. The final spectral profile is shown in Figure 1. From this, we find a CO( $J = 2 \rightarrow 1$ ) luminosity of  $L'_{\text{CO}(J=2\rightarrow 1)} = (6.0 \pm 0.5) \times 10^{10}$  K km s<sup>-1</sup> pc<sup>2</sup>. Assuming a brightness temperature ratio of  $r_{21} = 0.76$  between the  $J = 2 \rightarrow 1$  and  $J = 1 \rightarrow 0$  transitions (Daddi et al. 2015), we find a CO( $J = 1 \rightarrow 0$ ) luminosity of  $L'_{\text{CO}(J=1\rightarrow 0)} = (7.8 \pm 0.7) \times 10^{10}$  K km s<sup>-1</sup> pc<sup>2</sup>.

### 3.2. HCN and HNC ( $J = 2 \rightarrow 1$ )

For each of the lines, a moment-0 map is made using the velocity range  $-230$  to  $360$  km s<sup>-1</sup> ( $\Delta\nu \sim 590$  km s<sup>-1</sup>), nearly identical to the FWZI velocity range for the CO( $J = 2 \rightarrow 1$ ) line, and the rms noise for each moment-0 map is calculated using the source-free pixels. We tentatively detect the HCN ( $J = 2 \rightarrow 1$ ) and HNC( $J = 2 \rightarrow 1$ ) lines (Figure 3), redshifted to  $\nu_{\text{obs}} = 80.704$  GHz and  $\nu_{\text{obs}} = 82.555$  GHz, respectively. Given the modest significance of our detections, we use the dirty cube to calculate integrated line fluxes, instead of the cleaned image cube, in order to avoid biases introduced by the cleaning process. We do not make any correction for flux in the side lobes of the dirty beam, given that the source is spatially unresolved. We perform a 2D Gaussian fit to the moment-0 maps of HCN and HNC emission in order to measure the line fluxes. We detect line emission at the source position at significances of  $3.0\sigma$  and  $2.4\sigma$  for HCN and HNC, with velocity-integrated line fluxes of  $I_{\text{HCN}} = 0.28 \pm 0.09$  Jy km s<sup>-1</sup> and  $I_{\text{HNC}} = 0.17 \pm 0.07$  Jy km s<sup>-1</sup>, respectively. These correspond to  $L'_{\text{HCN}(J=2\rightarrow 1)} \sim (9 \pm 3) \times 10^9$  K km s<sup>-1</sup> pc<sup>2</sup> and  $L'_{\text{HNC}(J=2\rightarrow 1)} \sim (5 \pm 2) \times 10^9$  K km s<sup>-1</sup> pc<sup>2</sup>. The HCN( $J = 2 \rightarrow 1$ ) luminosity is extrapolated to the HCN( $J = 1 \rightarrow 0$ ) luminosity using a brightness temperature ratio of  $r_{21} \sim 0.65$  (Krips et al. 2008; Geach & Papadopoulos 2012) between the  $J = 2 \rightarrow 1$  and  $J = 1 \rightarrow 0$  transitions (see Section 5.3.2 for a discussion of how this impacts our results), which yields  $L'_{\text{HCN}(J=1\rightarrow 0)} \sim (1.4 \pm 0.5) \times 10^{10}$  K km s<sup>-1</sup> pc<sup>2</sup>.

We use the same methodology as above to obtain upper limits on HCO<sup>+</sup>( $J = 2 \rightarrow 1$ ), HC<sub>3</sub>N( $J = 20 \rightarrow 19$ ), and H<sub>2</sub>O( $3_{13} \rightarrow 2_{20}$ ) emission. We find  $I \lesssim 0.2$  Jy km s<sup>-1</sup> pc<sup>2</sup> for each of the lines, yielding line luminosities  $L' < 7\text{--}8 \times 10^9$  K km s<sup>-1</sup> pc<sup>2</sup> (Table 1). These limits are consistent with the limits derived from stacking, as described in Section 4.1. No continuum emission was detected in the CO or dense gas observations, and we set a  $3\sigma$  upper limit of  $<0.3$  mJy beam<sup>-1</sup> on the continuum flux of the source at an observed frame wavelength of 3 mm.

## 4. Analysis

### 4.1. Stacking of Dense Gas Tracers

Since both the HCN and HNC lines are only tentatively detected at  $\lesssim 3\sigma$  significance, we stack these lines together using both image- and  $uv$ -plane stacking to further investigate the reliability of their detection. We stack 200 velocity channels ( $\sim 2900$  km s<sup>-1</sup>) around the predicted line peaks (using  $\nu_{\text{obs}}$  from Table 1 and  $z = 1.197$ ) for the HCN and HNC

( $J = 2 \rightarrow 1$ ) lines. For stacking in the visibility plane, the visibilities  $V(u, v)$  are concatenated after the  $u, v$  values are scaled by  $\nu_i/\nu_0$ , where  $\nu_i$  is the frequency of channel  $i$ , and  $\nu_0$  is the central frequency of observation. Dirty maps from the stacked visibilities are made using UV\_MAP. For image-plane stacking, the dirty spectral cubes for individual lines are stacked over the same channel width, centered on the expected HCN and HNC line centers.

The spectral cubes, following both  $uv$ -plane and image-plane stacking, are binned over the velocity range  $\Delta\nu \sim 590$  km s<sup>-1</sup> around the central channel, assuming that the velocity widths of CO, HCN, and HNC are the same. Consistency between the two methods is validated by comparing the rms noise achieved after stacking. In addition, the weighted average of HCN and HNC line fluxes, as estimated in Section 3.2, is consistent with the line flux detected in the stacked HCN and HNC emission map. The resulting map (Figure 3) has an rms noise of  $\sim 0.1$  mJy beam<sup>-1</sup>, and an unresolved source is detected at the CO and optical position of EGS 13004291, with a peak flux of 0.4 mJy and at a  $4\sigma$  significance.

To ensure the validity of the approach, the same stacking routine is performed using central channels that have been randomly selected, rather than centered on known line positions. Dirty maps are made from the stacked visibilities and searched for significant features. The rms noise is calculated per channel. The number of features found is consistent with the distribution of the peak of a set of generated Gaussian images with an rms noise of 0.1 mJy beam<sup>-1</sup> in each channel, as checked using a two-sided Kolmogorov–Smirnov test. In a further 1000 trials, no features at an equal or higher significance are found within a synthesized beam size located at the central pixel.

Finally, we also attempted to stack other dense gas tracers with HCN, and we found that the significance of the detection is reduced in the stacked images. Removing the HCN contribution to the stacked image, we obtain  $3\sigma$  upper limits on the HCO<sup>+</sup>, HC<sub>3</sub>N, and H<sub>2</sub>O line fluxes, consistent with those determined in Section 3.2. We emphasize that for all of our dense gas observations, we use stacking to confirm our results; however, our line fluxes and upper limits are determined for each dense gas tracer individually, as described in Section 3.2.

### 4.2. Blind Line Search by Matched Filtering

Given the large bandwidth of the WideX correlator, we perform blind matched filtering on the reduced HCN image cube to search for other spectral lines in the primary beam. We use the code developed by R. Pavesi et al. (2017, in preparation), which performs a blind search for spectral line features in interferometric data cubes. For a given source spatial extent and spectral line width, we generate a template spectral cube, assuming a 2D circular Gaussian to describe the source structure and a 1D Gaussian to describe the spectral line. Due to the spatial correlation of the noise, inherent in interferometric images, the source size is not trivially identical to the “optimal” template size, but requires smaller templates instead (see Pavesi et al. for details). We then convolve the templates defined in this way with the observed data cube, and the resulting cube is then searched for significant features.

We perform the search for a range of possible template spatial sizes ( $5'' < \Delta x < 17''$ ) and velocity widths ( $100$  km s<sup>-1</sup>  $\lesssim \Delta\nu \lesssim 500$  km s<sup>-1</sup>). While the same spectral feature might be

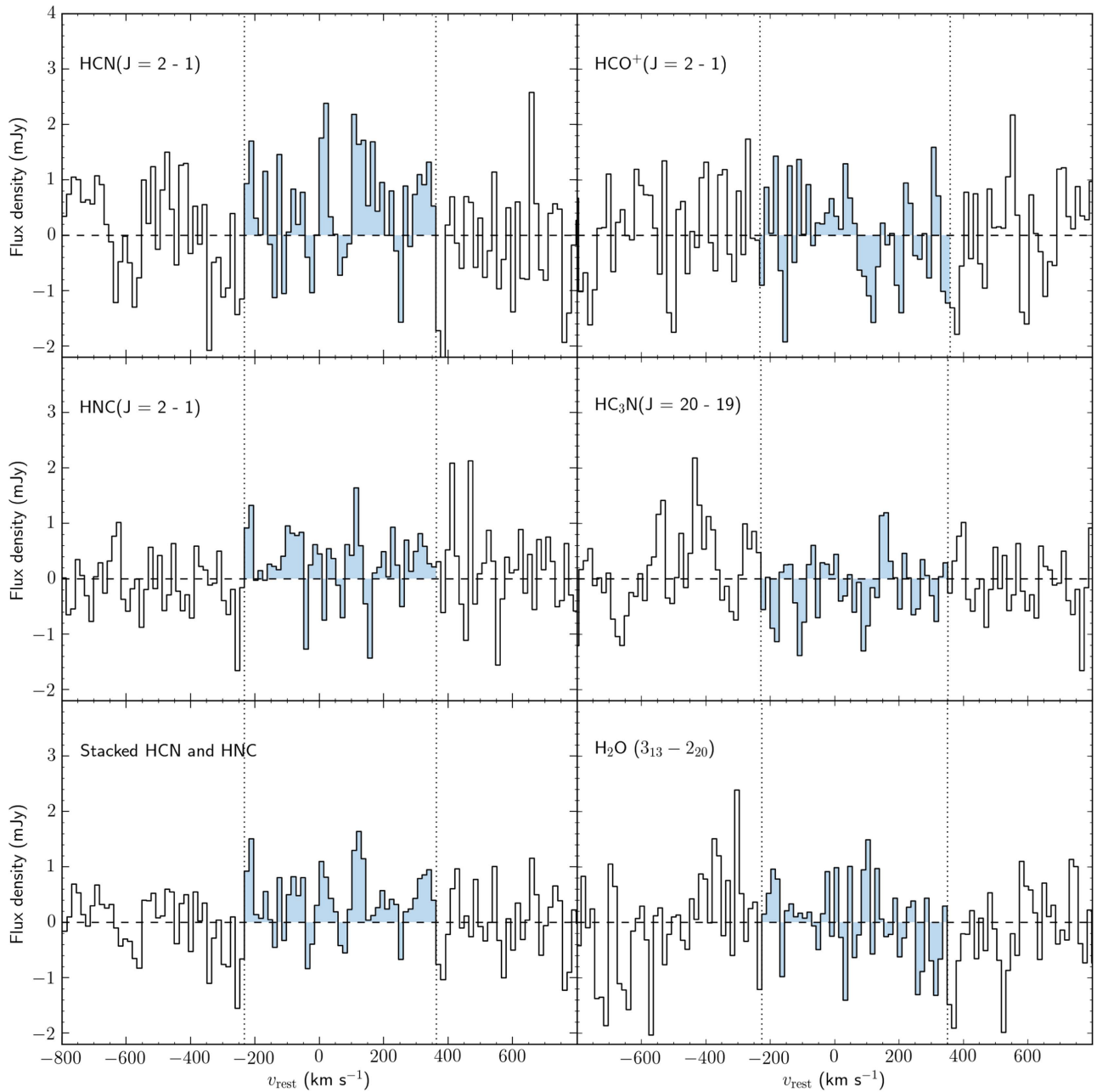


**Figure 2.** Observed spectra for HCN (top left), HNC (middle left), stacked HCN and HNC emission (bottom left),  $\text{HCO}^+$  (top right),  $\text{HC}_3\text{N}$  (middle right), and  $\text{H}_2\text{O}$  (bottom right). We tentatively detect HCN and HNC emission at  $\sim 3\sigma$  and  $\sim 2.4\sigma$  significances, respectively. By stacking the HCN and HNC lines together, we detect emission at  $\sim 4\sigma$  significance. The other dense gas tracers including  $\text{HCO}^+$ ,  $\text{HC}_3\text{N}$ , and  $\text{H}_2\text{O}$  remain undetected. The dotted vertical lines show the regions used to calculate the velocity-integrated line fluxes (or upper limits).

detected at high significance in multiple templates with varying spatial extents, we expect the highest signal-to-noise ratio (S/N) when the source extent (after convolving with the telescope beam) “matches” the template size, and we therefore select the most significant detection of the source among all the templates. Finally, we obtain the spatial coordinates, peak channel, and significance of the features with the highest S/N. We visually check this list of features, removing obvious contaminants such as bad channels and those features that occur at the edge of the image or of the spectral band. Finally, we check the remaining putative features for counterparts in the 3D-HST WFC3-selected photometric catalog of the AEGIS field and the multiwavelength AEGIS catalog (Davis

et al. 2007; Whitaker et al. 2011; Brammer et al. 2012; Skelton et al. 2014). Here we discuss the two most likely candidates, both of which are detected at  $\geq 6\sigma$  significance.

#### 4.2.1. EGS J141917.4+524922

We detect a spectral feature at nearly  $\sim 7\sigma$  significance at  $\nu_{\text{obs}} = 82.289$  GHz. We fit the spectrum with a 1D Gaussian (Figure 4). We find a FWHM velocity width of  $\Delta v_{\text{FWHM}} = 481 \pm 112$  km s $^{-1}$  (Table 2). We fit a 2D Gaussian to the moment-0 map for our detected spectral feature to obtain the peak emission position (J2000 R.A.:  $14^{\text{h}}19^{\text{m}}17^{\text{s}}.406$ , decl.:  $52^{\text{d}}49^{\text{m}}21^{\text{s}}.155$ ), which corresponds to a distance of  $23''.9$  from

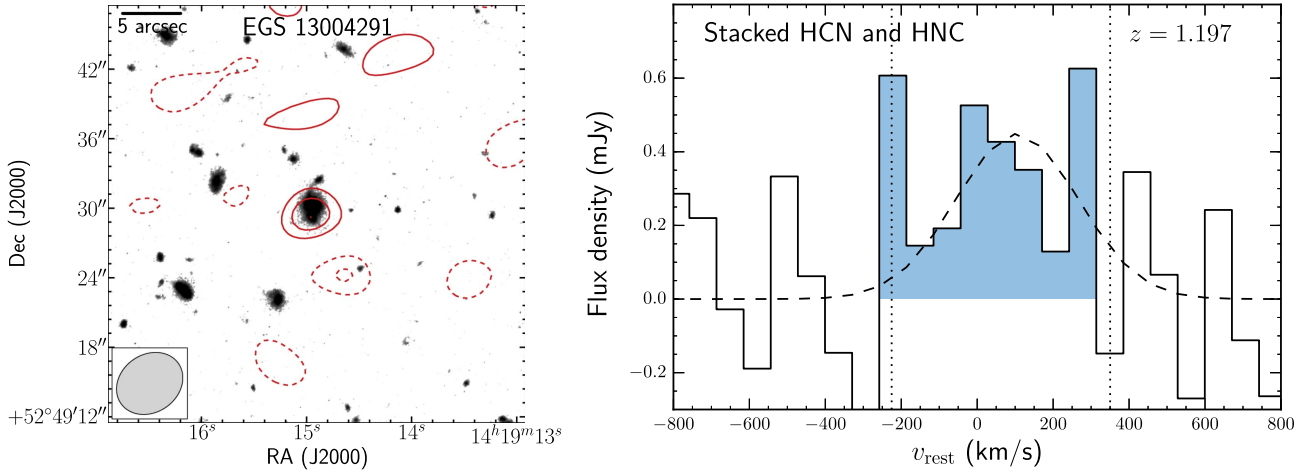


**Figure 3.** Stacked HCN and HNC emission, made by collapsing the reduced and cleaned stacked cube along the frequency axis over the velocity range  $-230$  to  $360 \text{ km s}^{-1}$  (shown as dotted lines in Figure 2) as for the CO( $2 \rightarrow 1$ ) line in EGS 13004291. The stacked emission is detected at a  $4\sigma$  significance, where  $1\sigma \sim 0.05 \text{ Jy km s}^{-1}$ . The  $\pm 2, 3, 4\sigma$  contours are overlaid on the 3D-HST  $H$ -band image (Brammer et al. 2012; Skelton et al. 2014). The synthesized beam has a size of  $\sim 6''0 \times 5''0$  and is indicated in the bottom left corner. Right: binned spectrum extracted from the stacked HCN and HNC cube, at the central pixel, with a velocity resolution of  $\sim 72 \text{ km s}^{-1}$ . The dashed line shows a single-component Gaussian fit to the data.

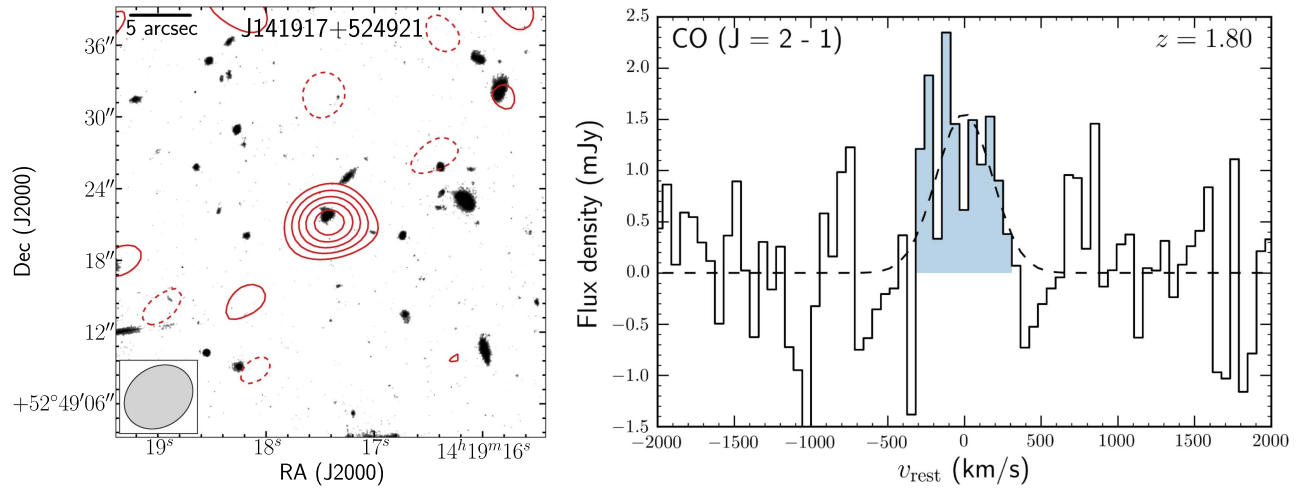


**Figure 4.** Left: moment-0 map for CO( $J = 2 \rightarrow 1$ ) emission from J141917+524922, a serendipitously detected ULIRG at  $z = 1.8$ ; the moment-0 image was made by integrating over the velocity range  $-295$  to  $273 \text{ km s}^{-1}$ . The source is detected at  $\sim 7\sigma$  significance, where  $1\sigma \sim 0.07 \text{ Jy km s}^{-1}$ . The contours at  $\pm 2, 3, 4, 5,$  and  $6\sigma$  significance have been overlaid on the 3D-HST  $H$ -band image. The synthesized beam has a size of  $\sim 6''0 \times 5''0$  and is indicated in the bottom left corner. The image is shown without primary beam correction. Right: spectral line profile extracted for J141917+524922 from the primary beam corrected spectral cube, at the peak pixel in the moment-0 map, with a velocity resolution of  $\sim 56 \text{ km s}^{-1}$ . The dashed line shows a single-component Gaussian fit to the spectral line.

**Table 2**  
Observation Summary for CO Lines

| Source         | $z$                 | Transition            | $\Delta v_{\text{FWHM}}$<br>( $\text{km s}^{-1}$ ) | $I_{\text{CO}}$<br>( $\text{Jy km s}^{-1}$ ) | $L'_{\text{CO}}$<br>( $10^{10} \text{ K km s}^{-1} \text{ pc}^2$ ) | References |
|----------------|---------------------|-----------------------|--|--|--|------------|
| EGS 13004291   | $1.1964 \pm 0.0001$ | $J = 2 \rightarrow 1$ | $340 \pm 32$                                       | $3.09 \pm 0.27$                              | $6.0 \pm 0.5$  | (1)        |
|                | 1.197               | $J = 3 \rightarrow 2$ | 311  | $4.6 \pm 0.1$                                | $3.9 \pm 0.1$  | (2)        |
| J141917+524921 | $1.8016 \pm 0.0002$ | $J = 2 \rightarrow 1$ | $481 \pm 112$                                      | $0.75 \pm 0.11$                              | $3.1 \pm 0.5$  | (1)        |
| J141912+524924 | $3.2206 \pm 0.0002$ | $J = 3 \rightarrow 2$ | $233 \pm 54$                                       | $0.59 \pm 0.09$                              | $3.0 \pm 0.5$  | (1)        |

**Note.** Details of observed CO transitions. (1) This work. (2) Tacconi et al. (2013).

the phase center of our observations. Based on the AEGIS source catalog and *Spitzer* IRAC and optical counterparts in the *HST*-CANDELS field, we identify EGS J141917.4+524922 as the nearest counterpart (hereafter J141917+524922). This source is classified as a starburst-dominated ULIRG in the literature, with a

known redshift of  $z = 1.80 \pm 0.02$  based on previously obtained *Spitzer* Infrared Spectrograph (IRS) spectroscopy (Huang et al. 2009). The detected emission thus is consistent with CO( $J = 2 \rightarrow 1$ ) emission at  $z = 1.8016 \pm 0.0002$ . Comparing our emission peak position to the optical  $H$ -band position for

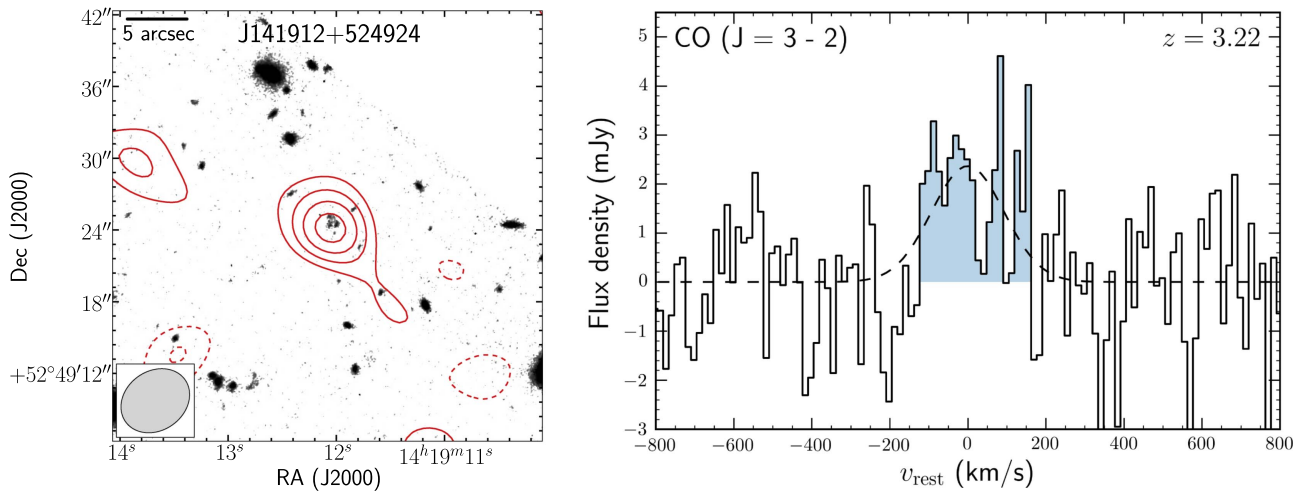


**Figure 5.** Left: moment-0 map for line emission from J141912+524924, an MS galaxy at  $z = 3.22$ . The line has been tentatively identified as CO( $J = 3 \rightarrow 2$ ). The moment-0 image was made by integrating over the velocity range  $-138$  to  $134 \text{ km s}^{-1}$ . The source is detected at  $\sim 6\sigma$  significance, where  $1\sigma \sim 0.05 \text{ Jy km s}^{-1}$ . The contours at  $\pm 2, 3, 4, 5,$  and  $6\sigma$  significance have been overlaid on the 3D-HST  $H$ -band image. Both the  $z_{\text{phot}}$  and our detected spectral feature are consistent with CO( $J = 3 \rightarrow 2$ ) line emission at  $z = 3.22$ . The synthesized beam has a size of  $\sim 6''.0 \times 5''.0$  and is indicated in the bottom left corner. The image is shown without primary beam correction. Right: spectral line profile extracted for J141912+524924 from the primary beam corrected spectral cube, at the peak pixel in the moment-0 map, with a velocity resolution of  $\sim 14 \text{ km s}^{-1}$ . The dashed line shows a single-component Gaussian fit to the spectral line.

J141917+524922, we find a spatial offset of  $\sim 0''.46 \pm 0''.41$ , which is much smaller than our beam size ( $6''.0 \times 5''.0$ ). We obtain a CO velocity-integrated line flux of  $I_{\text{CO}} = 0.75 \pm 0.11 \text{ Jy km s}^{-1}$ , after correcting for the primary beam response (Table 2).

#### 4.2.2. EGSIRAC J141912.03+524924.0

We detect a spectral feature at  $\sim 6.5\sigma$  significance at  $\nu_{\text{obs}} = 81.930 \text{ GHz}$ . We fit the spectrum with a 1D Gaussian (Figure 5). We find an FWHM velocity width of  $\Delta\nu_{\text{FWHM}} \sim 233 \pm 54 \text{ km s}^{-1}$  (Table 2). We fit a 2D Gaussian to the moment-0 map for our detected spectral feature to obtain the peak emission position (J2000 R.A.:  $14^{\text{h}}19^{\text{m}}12^{\text{s}}.088$ , decl.:  $52^{\circ}49^{\text{m}}24^{\text{s}}.235$ ), which corresponds to a distance of  $27''$  from the phase center of our observations. Based on the AEGIS and the 3D-HST/CANDELS catalogs for the AEGIS field, we identify EGSIRAC J141912.03+524924.0 as the nearest counterpart (hereafter J141912+524924). Comparing the emission peak position to the optical  $H$ -band position for J141912+524924, we find an offset of  $\sim 0''.57 \pm 0''.55$ , which is much smaller than our beam size ( $6''.0 \times 5''.0$ ).

Unfortunately, there is no known redshift for this source to allow for immediate spectroscopic confirmation, although it has photometric coverage as part of the AEGIS catalog (Whitaker et al. 2011). We therefore use the photometric redshift code EAZY (Brammer et al. 2008) to estimate a photometric redshift of  $z_{\text{phot}} \sim 3.23$ . We test the robustness of this estimate using a variety of different population synthesis models and find  $2.6 < z_{\text{phot}} < 4.2$ . The emission feature thus is most consistent with the CO( $J = 3 \rightarrow 2$ ) line at  $z = 3.2206 \pm 0.0002$ . We obtain a velocity-integrated line flux of  $I_{\text{CO}} = 0.59 \pm 0.09 \text{ Jy km s}^{-1}$ , after correcting for the primary beam response (Table 2).

#### 4.3. SED Fitting

We perform SED fitting for all our detected sources using both CIGALE (Code Investigating GALaxy Emission; Noll et al. 2009; Serra et al. 2011) and the high- $z$  extension of

MAGPHYS (Multi-wavelength Analysis of Galaxy Physical Properties; da Cunha et al. 2008, 2015). We use all available photometric data points for each of the sources, as described in Section 2.2. *Herschel*/PACS and *Herschel*/SPIRE fluxes from the NMBS are available only for EGS 13004291 and J141917+524921, as J141912+524924 is not detected. We used the deblended *Herschel* fluxes from the NMBS (Whitaker et al. 2011). Since the two serendipitously detected sources are at distances of  $23''$  and  $27''$  from EGS 13004291, respectively, and can potentially contaminate its SPIRE fluxes (SPIRE beam size at  $350 \mu\text{m} \sim 24''$ ), the *Herschel* Interactive Processing Environment (HIPE) software package was used to examine the photometric images. The HIPE tasks SourceExtractorTimeline and source extractors were used to ensure that the deblended FIR fluxes were not contaminated.

CIGALE builds galaxy SEDs from UV to radio wavelengths assuming a combination of modules. These allow us to model the star formation history (SFH), the stellar emission using population synthesis models (Bruzual & Charlot 2003; Maraston 2005), nebular lines, dust attenuation (e.g., Calzetti et al. 2000), dust emission (e.g., Draine & Li 2007; Casey 2012), contribution from an AGN (Fritz et al. 2006; Dale et al. 2014), and radio emission. The SEDs are built while maintaining consistency between UV dust attenuation and FIR emission from the dust. We use simple analytical functions to model the star formation histories—a double exponentially decreasing SFH, and a delayed SFH. We use the dust attenuation from Calzetti et al. (2000) and the dust emission models from Dale et al. (2014). Finally, CIGALE performs a probability distribution function analysis for our specified model parameters and obtains the likelihood-weighted mean value for each.

MAGPHYS similarly uses a Bayesian approach to constrain galaxy-wide physical properties, including the star formation rate, stellar and dust mass, and dust temperature. It builds a large library of reference spectra with different star formation histories (using stellar population synthesis models from Bruzual & Charlot 2003) and dust attenuation properties (using models from Charlot & Fall 2000). It also ensures energy

balance between the optical and UV extinction and the FIR emission due to dust.

In order to account for possible AGN contamination in our FIR-luminous sources, we carry out SED fitting with both CIGALE and MAGPHYS for EGS 13004291 and J141917+524922. EGS 13004291 has been detected in the 0.5–2 keV soft X-ray band in deep *Chandra* observations of the AEGIS field (Laird et al. 2009; Nandra et al. 2015), raising the possibility that an AGN may be present and that it may contribute to the galaxy’s FIR luminosity. However, we can rule out the presence of an AGN for two reasons. First, the galaxy is consistent with the FIR–X-ray correlation (Symeonidis et al. 2011). Second, the hardness ratio of the X-ray emission indicates a starburst origin of the X-ray emission rather than an AGN (Symeonidis et al. 2014). We further test for the presence of an AGN in both our sources by including the fractional contribution of an AGN to the IR luminosity as a free parameter in SED fitting with CIGALE; no good fit is found with a nonzero AGN contribution.

SED fits found using MAGPHYS and CIGALE were consistent within the errors for EGS 13004291 and J141917+524924. We did not find a good fit for the dust peak for J141917+524922 using MAGPHYS. The best-fit SEDs from CIGALE are shown in Figure 6, and the corresponding fit parameters are listed in Table 3. The  $L_{\text{FIR}}$  for all sources was obtained by integrating the area under the best-fit SED over  $\lambda_{\text{rest}} = 42.5\text{--}122.5 \mu\text{m}$ , and  $L_{\text{IR}}$  was obtained by integrating over  $\lambda_{\text{rest}} = 8\text{--}1000 \mu\text{m}$  (Casey et al. 2014).

#### 4.4. Comparison with Literature Values

We compare our SED-fitting-derived physical parameters (Table 3) against those available in the literature. For EGS 13004291, Tacconi et al. (2013) have derived a star formation rate of  $\text{SFR} \sim (630 \pm 220) M_{\odot} \text{yr}^{-1}$  and a stellar mass of  $M_{*} \sim (9.3 \pm 2.8) \times 10^{10} M_{\odot}$ . These values were obtained using an extinction-corrected  $24 \mu\text{m}$  derived IR luminosity + UV flux. However, Freundlich et al. (2013) derive an  $\text{SFR} \sim 182 M_{\odot} \text{yr}^{-1}$ , using the optical [O II] line luminosity, and a stellar mass of  $M_{*} \sim 5.0 \times 10^{11} M_{\odot}$ . They add the caveat that this method is likely to underestimate the SFR, since it does not account for dust-embedded star-forming regions.

Our derived properties from CIGALE depend significantly on the assumed SFH for EGS 13004291. Assuming a stellar history including a young stellar population from recent starburst activity, we find an  $\text{SFR} \sim 714 \pm 42 M_{\odot} \text{yr}^{-1}$ , averaged over the last 10 Myr, and a stellar mass of  $M_{*} \sim 1.0 \times 10^{11} M_{\odot}$ . Using only the  $L_{\text{FIR}}$  as a star formation indicator (Kennicutt 1998), we obtain an  $\text{SFR} \sim 220 M_{\odot} \text{yr}^{-1}$ , which is comparable to the SFR obtained using UV emission; the sum of the SFRs obtained from UV and FIR emission is then roughly consistent with the SFR from SED fitting.

For EGS 141917+524922, previous SED fitting has been performed to the IR and radio photometry (Huang et al. 2009), on which basis it was classified as a starburst-dominated ULIRG. Our stellar mass of  $M_{*} \sim (2.5 \pm 0.2) \times 10^{11}$  is consistent with the literature value of  $M_{*} \sim 3 \times 10^{11}$ . However, we find  $L_{\text{IR}} \sim (9 \pm 3) \times 10^{11} L_{\odot}$ , which is  $5\times$  lower than the literature value. We expect the uncertainties on our estimate to be smaller due to better constraints on the IR luminosity provided by the *Herschel*/SPIRE photometry, which samples the peak of the FIR emission. Using only the  $L_{\text{FIR}}$ , we obtain an  $\text{SFR} \sim 96 M_{\odot} \text{yr}^{-1}$ , while we obtain an  $\text{SFR} \sim (384 \pm 40) M_{\odot} \text{yr}^{-1}$  from

SED fitting; as the SED fitting incorporates both the UV and FIR photometry, this implies that the dust-obscured star formation plays a relatively minor role.

Similarly for EGS 141912+524924, we find an  $\text{SFR} \sim 30 M_{\odot} \text{yr}^{-1}$  using only the  $L_{\text{FIR}}$ ; this is significantly smaller than the SFR estimated using complete optical photometric data  $\text{SFR} (\sim 110 \pm 7) M_{\odot} \text{yr}^{-1}$ , indicating that most of the star formation is not dust-obscured.

## 5. Discussion

### 5.1. CO Excitation in EGS 13004291

The quiescent mode of gas consumption in SFGs at high redshifts can result in markedly different molecular gas excitation than in the ULIRG/SMG/QSO population at comparable redshifts. While some SMGs show a low-excitation molecular gas component (e.g., Ivison et al. 2011; Riechers et al. 2011b), and although there is significant scatter in their excitation properties (e.g., Sharon et al. 2016), the CO excitation of the brightest ULIRGs and SMGs can be nearly thermalized up to  $J = 3$ , and mid- $J$  CO lines can be used to trace the bulk of the molecular gas, which is in a warm dense medium in many of these galaxies (e.g., Riechers et al. 2006b, 2009a, 2013). However, the bulk of the molecular gas in MS galaxies lies in extended, cold, diffuse gas reservoirs and can be most reliably traced using low-excitation molecular gas lines, as shown by the subthermal CO excitation prevalent in BzK galaxies (massive, optically selected SFGs at high redshift; see Dannerbauer et al. 2009; Daddi et al. 2010a, 2015). For a limited sample of BzK galaxies, there is also evidence for the presence of an additional warm and dense molecular gas component, resulting in significant  $\text{CO}(J = 5 \rightarrow 4)$  emission, which has been suggested to result from giant, dense starbursting clumps (Freundlich et al. 2013; Bournaud et al. 2015; Daddi et al. 2015). However, the observed warm, dense molecular gas component traced by high- $J$  CO lines does not encompass the cold, dense molecular gas traced by low- $J$  HCN emission, which is critical for star formation.

We measure the velocity-integrated line intensity for  $\text{CO}(J = 2 \rightarrow 1)$  to be  $I_{\text{CO}(J=2\rightarrow 1)} = 3.09 \pm 0.27 \text{ Jy km s}^{-1}$ , resulting in a line luminosity of  $L'_{\text{CO}(J=2\rightarrow 1)} = (6.0 \pm 0.5) \times 10^{10} \text{ K km s}^{-1} \text{ pc}^2$  (Figure 1). Based on the  $L'_{\text{CO}(J=3\rightarrow 2)}$  value in the literature (Tacconi et al. 2013), we obtain a brightness temperature ratio of  $r_{32} \sim 0.65 \pm 0.15$ . This is consistent with the average  $r_{32} = 0.58 \pm 0.16$  for high- $z$  BzK galaxies (Aravena et al. 2014; Daddi et al. 2015), all of which show significantly subthermal molecular gas excitation at  $J \geq 3$ . This is, however, in sharp contrast to high- $z$  ULIRGs such as the Cloverleaf quasar and F10214+4724, which display a molecular gas excitation consistent with a single high-temperature medium; that is, the CO rotational lines are thermalized to high- $J$  values ( $r_{32} \sim 1$ ; Riechers et al. 2011a).

The conversion factor  $\alpha_{\text{CO}}$  used to derive the molecular gas mass from the CO line luminosity generally depends on the metallicity, the average gas density, the relative fractions of warm and cold dense gas, and the gas excitation in each source (see Solomon & Vanden Bout 2005; Bolatto et al. 2013; Carilli & Walter 2013, for reviews), and different values are appropriate for ULIRGs as opposed to normal SFGs. Here, we attempt to determine the most appropriate  $\alpha_{\text{CO}}$  for EGS 13004291, based on its dynamical mass. We obtain an estimate



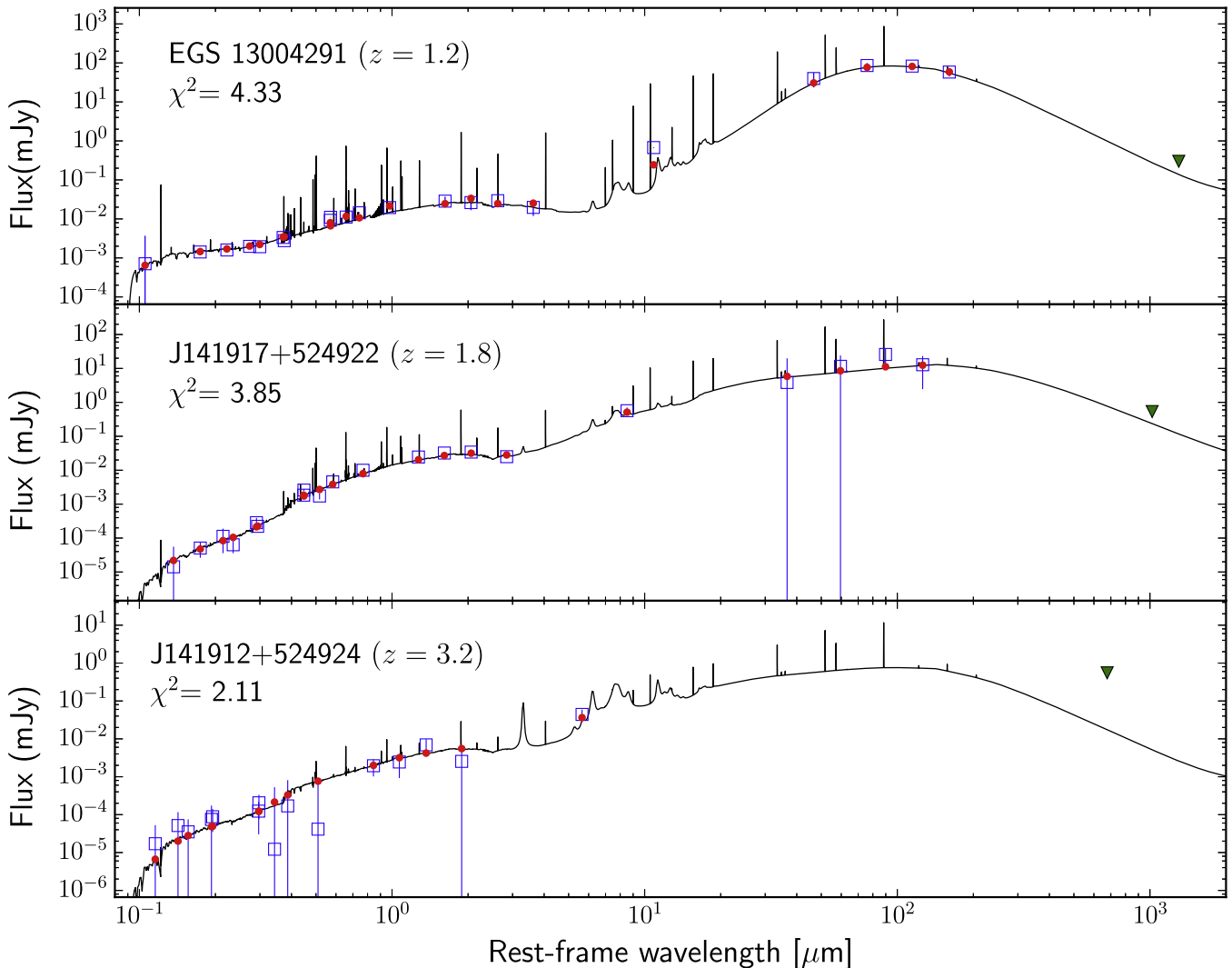


**Figure 6.** Best-fit SEDs (black lines) for EGS 13004291 (top), J141917+524922 (middle), and J141912+524924 (bottom) derived using CIGALE. The blue squares represent the archival photometry up to an observed frame wavelength of  $500 \mu\text{m}$ , and the red points represent the predicted model luminosities at the same wavelengths. The green triangles represent our new  $3\sigma$  upper limits derived from the 3 mm continuum observations.

for the dynamical mass based on our observed FWHM velocity width  $\Delta v_{\text{FWHM}} = 340 \pm 40 \text{ km s}^{-1}$  and the previously observed CO( $J = 3 \rightarrow 2$ ) half-light radius  $r_{1/2} = 3.9 \pm 1.0 \text{ kpc}$ , as determined by Tacconi et al. (2013). In addition, we consider the source morphology and orientation. The position–velocity (PV) diagrams for EGS 13004291, using both optical [O II] and CO spectral line observations, appear to show a disk-like velocity profile (Freundlich et al. 2013). Assuming a disk-like structure for EGS 13004291, we use a 2D Gaussian fitting to the optical *HST* *H*-band image to find an axial ratio of  $b/a \sim 0.7$ , that is,  $\sin^2(i) \sim 0.5$ . We then assume a dynamical mass model for a rotating disk, which can be described by  $M_{\text{dyn}} \sin^2(i) = 233.5 r_{1/2} (\Delta v_{\text{FWHM}})^2$ , where  $\Delta v_{\text{FWHM}}$  is in  $\text{km s}^{-1}$  and  $r_{1/2}$  is the half-light radius of the molecular disk in pc (Solomon & Vanden Bout 2005). We thus obtain a dynamical mass of  $M_{\text{dyn}} = (21 \pm 15) \times 10^{10} M_{\odot}$ .

Based on the relation between the dynamical mass within the half-light radius, gas mass, and the assumed dark matter (DM) mass,  $M_{\text{dyn}} = 0.5(M_{*} + M_{\text{gas}}) + M_{\text{DM}}$  (Daddi et al. 2010b), we then calculate the gas mass to be  $M_{\text{gas}} = (22 \pm 15) \times 10^{10} M_{\odot}$  (assuming that DM contributes 25% to the dynamical mass). This implies a CO luminosity to  $\text{H}_2$  gas mass conversion factor

of  $\alpha_{\text{CO}} \sim (2.8 \pm 2.0) M_{\odot} (\text{K km s}^{-1} \text{pc}^2)^{-1}$ , consistent with the  $\alpha_{\text{CO}} = 3.6 M_{\odot} (\text{K km s}^{-1} \text{pc}^2)^{-1}$  typically used for high- $z$  MS galaxies (e.g., Daddi et al. 2015).

However, we caution that the use of the dynamical mass to estimate  $\alpha_{\text{CO}}$  suffers from systematic uncertainties resulting from the dynamical estimator used. For example, if we assume an isotropic virial estimator (e.g., Pettini et al. 2001; Binney & Tremaine 2008; Engel et al. 2010)

$$M_{\text{dyn}}(r < r_{1/2}) = 190 r_{1/2} (\Delta v_{\text{FWHM}})^2 \quad (1)$$

using a normalization for a rotating disk at an average inclination such that  $\sin^2(i) = 0.25$  (see Bothwell et al. 2010; Engel et al. 2010), we obtain a dynamical mass of  $M_{\text{dyn}} = (8.5 \pm 6.1) \times 10^{10} M_{\odot}$  within  $r_{1/2} \sim 3.9 \text{ kpc}$ , which implies a gas mass of  $M_{\text{gas}} = (2.8 \pm 2.0) \times 10^{10} M_{\odot}$  and a conversion factor of  $\alpha_{\text{CO}} = (0.4 \pm 0.3) M_{\odot} (\text{K km s}^{-1} \text{pc}^2)^{-1}$ . This is more consistent with the values typically found in SMGs and nearby ULIRGs,  $\alpha_{\text{CO}} = 0.8 M_{\odot} (\text{K km s}^{-1} \text{pc}^2)^{-1}$  (e.g., Downes & Solomon 1998; Hodge et al. 2012; Riechers et al. 2014). Adjusting the above calculation to our inclination such that  $\sin^2(i) = 0.5$  would further decrease the  $M_{\text{dyn}}$  by a factor of  $\times 2$ , which would be inconsistent with our stellar mass

**Table 3**  
SED-fitting Results and Other Physical Parameters

| Source         | $z$   | $L_{\text{FIR}}$<br>( $10^{11} L_{\odot}$ ) | $M_{\text{dust}}$<br>( $10^9 M_{\odot}$ ) | $M_{\text{gas}}$<br>( $10^{11} M_{\odot}$ ) | $M_{*}$<br>( $10^{11} M_{\odot}$ ) | SFR<br>( $M_{\odot} \text{ yr}^{-1}$ ) | sSFR<br>( $\text{Gyr}^{-1}$ ) | $\delta_{\text{GDR}}$ | $f_{\text{gas}}$ |
|----------------|-------|---|---|---|------------------------------------|--|-------------------------------|-----------------------|------------------|
| EGS 13004291   | 1.197 | $12.57 \pm 4.2$                             | $2.4 \pm 0.2$                             | $2.8 \pm 0.3$                               | $1.0 \pm 0.1$                      | $714 \pm 42$                           | $6.8 \pm 0.7$                 | $117 \pm 21$          | 0.74             |
| J141917+524922 | 1.802 | $3.15 \pm 1.1$                              | $3.7 \pm 3.6$                             | $1.5 \pm 0.2$                               | $2.5 \pm 0.2$                      | $384 \pm 40$                           | $1.6 \pm 0.5$                 | $40 \pm 44$           | 0.37             |
| J141912+524924 | 3.221 | $1.69 \pm 0.5$                              | $0.7 \pm 0.5$                             | $2.6 \pm 0.4$                               | $0.5 \pm 0.1$                      | $110 \pm 7$                            | $2.2 \pm 0.3$                 | $380 \pm 342$         | 0.83             |

**Notes.**  $L_{\text{FIR}}$  is calculated by integrating the best-fit SED model over  $\lambda_{\text{rest}} = 42.5\text{--}122.5 \mu\text{m}$ . The gas masses were calculated using  $\alpha_{\text{CO}} = 3.6 M_{\odot} (\text{K km s}^{-1} \text{pc}^2)^{-1}$  (see Section 5.2) and the luminosities listed in Table 1, assuming brightness temperature ratios of  $r_{21} = 0.76$  and  $r_{32} = 0.42$ .

**Table 4**  
Comparison of Source Properties

| Source                     | $L_{\text{FIR}}/L'_{\text{HCN}}$<br>( $L_{\odot}/L_i$ ) <sup>a</sup> | $L_{\text{FIR}}/L'_{\text{CO}}$<br>( $L_{\odot}/L_i$ ) <sup>a</sup> | $L'_{\text{HCN}}/L'_{\text{CO}}$ |
|----------------------------|--|---|----------------------------------|
| EGS 13004291               | $90 \pm 30$  | $16 \pm 5$  | $0.17 \pm 0.07$                  |
| Other high- $z$ galaxies:  |  |   |                                  |
| F10214+4724                | $2600 \pm 550$   | $523 \pm 130$   | $0.18 \pm 0.04$                  |
| Cloverleaf                 | $1300 \pm 300$   | $135 \pm 33$  | $0.10 \pm 0.02$                  |
| Averages:                  |  |   |                                  |
| high- $z$ (U)LIRGs (5)     | $1667 \pm 688$   | $251 \pm 129$   | $0.16 \pm 0.07$                  |
| $z \approx 0$ ULIRGs (5)   | $1347 \pm 264$   | $148 \pm 33$  | $0.13 \pm 0.03$                  |
| $z \approx 0$ LIRGs (85)   | $829 \pm 791$  | $40 \pm 70$   | $0.05 \pm 0.04$                  |
| $z \approx 0$ spirals (45) | $618 \pm 395$  | $23 \pm 23$   | $0.04 \pm 0.02$                  |

**Note.**

<sup>a</sup>  $L_i = \text{K km s}^{-1} \text{pc}^2$ ; average values were calculated from the archival data as described in Section 2.2.

$M_{*} \sim 1.0 \times 10^{11} M_{\odot}$ . This discrepancy in  $M_{\text{dyn}}$  estimates highlights the systematic uncertainties inherent to dynamical mass computations. Motivated by the constraints on the dust-to-gas mass ratio as discussed in Section 5.2, we adopt  $\alpha_{\text{CO}} = 3.6 M_{\odot} (\text{K km s}^{-1} \text{pc}^2)^{-1}$ . This is consistent with the  $\alpha_{\text{CO}}$  derived for PHIBSS galaxies (including EGS 13004291) by Carleton et al. (2016) under the assumption of a constant gas depletion timescale.

### 5.2. Derived Properties from SED Fitting

We here use the SFR,  $M_{*}$ ,  $M_{\text{dust}}$  from the SED fitting (see Table 3), and the  $M_{\text{gas}}$  determined from our CO observations to compare our sources to the galaxy MS at their respective redshifts. We use the  $\text{sSFR}/\text{sSFR}_{\text{MS}}$ , the gas-to-dust mass ratio  $\delta_{\text{GDR}}$ , and the gas fraction  $f_{\text{gas}}$  as diagnostics, where  $\text{sSFR}_{\text{MS}}$  is the predicted sSFR for the galaxy MS at the source redshift (Whitaker et al. 2012),  $\delta_{\text{GDR}} = M_{\text{gas}}/M_{\text{dust}}$ , and  $f_{\text{gas}}$  is defined as

$$f_{\text{gas}} = \frac{M_{\text{gas}}}{M_{\text{gas}} + M_{*}}. \quad (2)$$

For EGS 13004291, we find an  $\text{sSFR}/\text{sSFR}_{\text{MS}} \sim 13 \pm 3$ , consistent with its classification as a starburst galaxy (Tacconi et al. 2013; Genzel et al. 2015). To estimate the dust temperature, we approximate the Draine & Li (2007) dust model by a blackbody multiplied by a power-law opacity and find a dust temperature of  $T_{\text{dust}} \approx 20U_{\text{min}}^{0.15} \sim 30 \text{ K}$ , where  $U_{\text{min}}$  is the best-fit intensity of the radiation field from SED fitting (Aniano et al. 2012). Assuming an  $\alpha_{\text{CO}} = 3.6 M_{\odot} (\text{K km s}^{-1} \text{pc}^2)^{-1}$ , we find a gas mass of  $M_{\text{gas}} = (2.8 \pm 0.3) \times 10^{11} M_{\odot}$  and a gas

fraction of  $f_{\text{gas}} \sim 0.74$ , consistent with the literature value ( $f_{\text{gas}} = 0.79$ ; Tacconi et al. 2013). We also find a gas-to-dust mass ratio of  $\delta_{\text{GDR}} \sim 120$ . Note that  $\delta_{\text{GDR}}$  strongly depends on the metallicity of the system (e.g., Leroy et al. 2011; Sandstrom et al. 2013; Rémy-Ruyer et al. 2014; Groves et al. 2015) and can vary significantly depending on the assumed dust properties, although typical values for high- $z$  galaxies are close to  $\delta_{\text{GDR}} \sim 100$  (Casey et al. 2014). For the  $z \sim 1.5$  MS galaxy BzK21000, a  $\delta_{\text{GDR}} \sim 104$  was found (Magdis et al. 2011). In low- and high-metallicity MS galaxies at  $z \sim 1.4$ , Seko et al. (2016) find  $\delta_{\text{GDR}} \sim 570$  and  $\delta_{\text{GDR}} \sim 400$ , respectively. However, their derived  $\delta_{\text{GDR}}$  may be lower by a factor of  $2 - 3 \times$  depending on the dust model assumed. Thus, the  $\delta_{\text{GDR}}$  in EGS 13004291 is consistent with that seen in  $z \sim 1\text{--}2$  gas-rich galaxies. Alternatively, if we were to assume an  $\alpha_{\text{CO}} = 0.8 M_{\odot} (\text{K km s}^{-1} \text{pc}^2)^{-1}$ , we would obtain a gas mass of  $M_{\text{gas}} = (6 \pm 1) \times 10^{10} M_{\odot}$ , a gas fraction of  $f_{\text{gas}} \sim 0.38$ , and a gas-to-dust mass ratio of  $\delta_{\text{GDR}} = 26 \pm 21$ , which is more consistent with the observed gas-to-dust mass ratio  $\delta_{\text{GDR}} \sim 40$  for dusty SMGs at high redshift (e.g., Santini et al. 2010; Bothwell et al. 2013; Swinbank et al. 2014; Zavala et al. 2015). Here,  $\alpha_{\text{CO}}$  varies inversely with the CO excitation temperature  $T_{\text{ex}}$  (Bolatto et al. 2013); that is, lower  $\alpha_{\text{CO}}$  values are more typically seen in sources such as SMGs and quasars, which also show higher CO excitation (Ivison et al. 2011; Carilli & Walter 2013), while EGS 13004291 displays subthermal CO excitation consistent with other MS galaxies at  $z \sim 1.5$  (Daddi et al. 2015). Therefore, we finally adopt an  $\alpha_{\text{CO}} = 3.6 M_{\odot} (\text{K km s}^{-1} \text{pc}^2)^{-1}$  for our  $M_{\text{gas}}$  and  $f_{\text{gas}}$  calculations (see Table 3).

For J141917+524922, we find an  $\text{sSFR}/\text{sSFR}_{\text{MS}} \sim 2.5$ , which is consistent with the galaxy MS at  $z = 1.8$  within the scatter (Genzel et al. 2015). This motivates our choice of  $\alpha_{\text{CO}} = 3.6 M_{\odot} (\text{K km s}^{-1} \text{pc}^2)^{-1}$ , instead of the value typically used for ULIRGs,  $\alpha_{\text{CO}} = 0.8 M_{\odot} (\text{K km s}^{-1} \text{pc}^2)^{-1}$ . Similarly, using a brightness temperature ratio  $r_{21} = 0.76$  (Daddi et al. 2015), we obtain a gas mass of  $M_{\text{gas}} = (1.5 \pm 0.2) \times 10^{11} M_{\odot}$  and a gas fraction of  $f_{\text{gas}} = 0.37$ , which is again consistent with the galaxy MS at  $z = 1.8$ . We obtain a gas-to-dust mass ratio of  $\delta_{\text{GDR}} = 40 \pm 44$ , which is consistent with the average value found for SMGs. The large uncertainties on the FIR fluxes of J141917+524922 result in a poorly constrained dust mass and therefore gas-to-dust ratio.

Applying similar diagnostics to J141912+524924, we find an  $\text{sSFR}/\text{sSFR}_{\text{MS}} \sim 0.8$ , making this source consistent with the galaxy MS at  $z = 3.22$ . J141912+524924 is then the highest-redshift unlensed MS galaxy detected to date. We find a gas-to-dust ratio  $\delta_{\text{GDR}} = 380 \pm 342$  and a gas fraction of  $f_{\text{gas}} \sim 0.83$ , implying that it is a gas-rich galaxy with possibly

low dust content. We emphasize that the lack of FIR photometry for this source leads to a poorly constrained dust mass and hence gas-to-dust ratio.

### 5.3. Comparison of Dense Gas Properties

We use the following set of diagnostics to characterize star formation in EGS 13004291: the fraction of dense, actively star-forming gas  $f_{\text{dense}} = M_{\text{dense}}/M_{\text{gas}} \propto L'_{\text{HCN}}/L'_{\text{CO}}$ , the global star formation efficiency of the molecular gas  $\text{SFE}_{\text{mol}} = \text{SFR}/M_{\text{gas}} \propto L_{\text{FIR}}/L'_{\text{CO}}$ , and the star formation efficiency of the dense gas  $\text{SFE}_{\text{dense}} = \text{SFR}/M_{\text{dense}} \propto L_{\text{FIR}}/L'_{\text{HCN}}$ . Unless explicitly stated, we calculate these ratios using line luminosities for the  $J = 1 \rightarrow 0$  transition, calculated in Sections 3.1, 3.2. We calculate  $L_{\text{FIR}}/L'_{\text{HCN}}$ ,  $L'_{\text{HCN}}/L'_{\text{CO}}$ , and  $L_{\text{FIR}}/L'_{\text{CO}}$  values for the sample of archival sources described in Section 2.2, and we compare our obtained values for EGS 13004291 against those for different galaxy populations using these diagnostics (see Table 4). Our sample of archival sources includes the Cloverleaf quasar and IRAS F10214+4724, which are among the best studied and brightest HCN and CO sources at high redshift. This allows us to place the properties of its star-forming environment in context. We do not compare our source to APM 08279+5255 at  $z = 3.9$ , the only other solid HCN detection at high redshift we have excluded this source despite detailed observations because of its unusual gas excitation properties (e.g., Weiß et al. 2007; Riechers et al. 2010b).

#### 5.3.1. Star Formation Models

Two main classes of dense gas star formation models have been proposed to explain the observed  $L_{\text{FIR}}-L'_{\text{HCN}}$  relation (see Figure 7, middle): threshold density models and turbulence-regulated star formation models. Threshold density models assume a fixed SFR per unit gas mass above a certain critical density, that is, a constant  $\text{SFE}_{\text{dense}}$ . Working under this assumption, the slope of the  $L_{\text{FIR}}-L'_{\text{HCN}}$  relation ( $\equiv \text{SFE}_{\text{dense}}$ ) is expected to remain constant, regardless of the star-forming environment or the galaxy type (Gao & Solomon 2004b; Wu et al. 2005, 2010).

On the other hand, turbulence-regulated star formation models predict that the SFR depends on the properties of the molecular gas cloud as a whole—the gas surface density, the pressure, and the turbulent velocity dispersion (e.g., Krumholz & McKee 2005; Krumholz & Thompson 2007). Based on these properties, they predict that different molecular gas tracers would produce different slopes in the  $L_{\text{FIR}}-\text{gas}$  luminosity plot. In their parameterization,  $\text{SFE}_{\text{mol}}$  is a function of both the local free-fall timescale,  $\tau_{\text{ff}}$ , and of the ISM turbulence represented by the Mach number  $\mathcal{M}$ . At a given  $\mathcal{M}$ , the SFE varies according to  $1/\tau_{\text{ff}}$ , and the SFR varies according to  $\bar{n}/\tau_{\text{ff}}$ , where  $\bar{n}$  is the average gas density. The observed  $\text{SFE}_{\text{mol}}$  then depends on how the critical density ( $n_{\text{crit}}$ ) of the tracer in question compares to  $\bar{n}$ , as this determines the local free-fall timescale; that is,  $\tau_{\text{ff}}$  will be smaller and  $\text{SFE}_{\text{mol}}$  will be higher in regions of large density contrasts. For CO observations, which trace all molecular gas, the average gas density is comparable to the critical density and  $\tau_{\text{ff}} \propto \bar{n}^{-0.5}$ , and the SFR  $\propto \bar{n}^{1.5}$ , which is close to the slope seen in the  $L_{\text{FIR}}-L'_{\text{CO}}$  relation. If the average gas density is much smaller than the tracer's critical density,  $\tau_{\text{ff}}$  is determined by  $n_{\text{crit}}$ , and

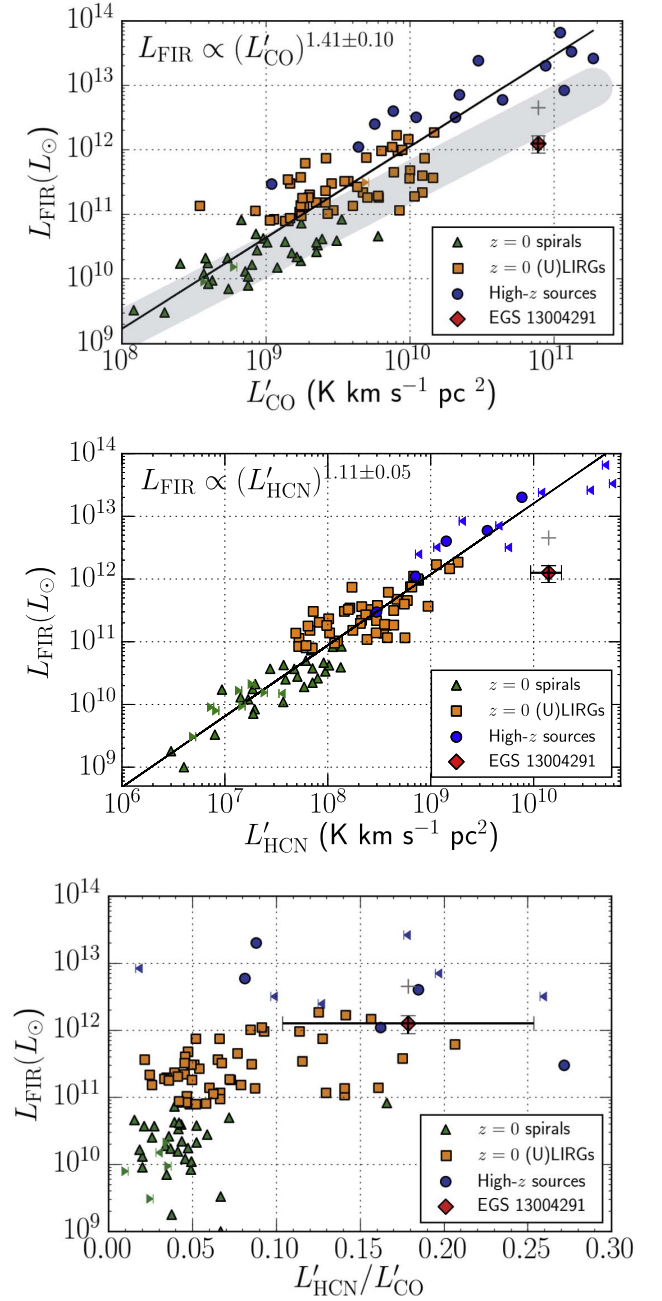


**Figure 7.**  $L_{\text{FIR}}-L'_{\text{CO}}$  (top),  $L_{\text{FIR}}-L'_{\text{HCN}}$  (middle), and  $L_{\text{FIR}}-f_{\text{dense}}$  (bottom) relations for the compiled archival data on a large sample of sources for which CO and HCN rotational lines have been observed and where IR photometric coverage exists, as described in Section 2.2. The values have been updated to the assumed cosmology; the green upper triangles represent the local spiral galaxy population (Gao & Solomon 2004b), the orange squares represent the updated values for (U)LIRGs (Graciá-Carpio et al. 2008; García-Burillo et al. 2012), and the blue circles represent all  $z > 1$  sources (Gao et al. 2007; Riechers et al. 2007); The left and right pointed triangles, with a vertical line on the right or left, are the upper/lower limits; the shaded region in the top plot shows the  $\pm 1\sigma$  region around the best fit to the galaxy main sequence (Genzel et al. 2010). The best-fit lines were derived using only the detections. The red diamond represents EGS 13004291, which lies below the best-fit line in  $L_{\text{FIR}}-L'_{\text{HCN}}$ , implying that EGS 13004291 has a lower  $\text{SFE}_{\text{dense}}$  when compared to this galaxy sample. The gray cross represents the source EGS 13004291, with an equivalent  $L_{\text{FIR}}$  that represents the total star formation, instead of only the dust-obscured star formation, enabling better comparison against the high- $z$  sources in our sample whose star formation is predominantly dust-obscured (see Section 5.3.4).

the SFE will be nearly constant; that is, the slope of the  $L_{\text{FIR}}-\text{gas}$  luminosity relation is close to unity, thus explaining the slope of the  $L_{\text{FIR}}-L'_{\text{HCN}}$  relation. Additionally, the SFE varies inversely with the Mach number  $\mathcal{M}$ ; that is, increased turbulence in the ISM hinders efficient star formation.

In this model,  $f_{\text{dense}}$  increases with both the average gas density  $\bar{n}$  and ISM turbulence, as a higher Mach number  $\mathcal{M}$  broadens the density probability distribution of  $f_{\text{dense}}$  and hence increases the mass of the dense gas above the critical density. Finally,  $\text{SFE}_{\text{mol}} = f_{\text{dense}} \times \text{SFE}_{\text{dense}}$ ; we can thus constrain  $\text{SFE}_{\text{dense}}$  using this model.

Observationally, the turbulence-regulated star formation scenario is favored. Merging ULIRGs at both high redshift and in the local universe display a higher  $L_{\text{FIR}}/L'_{\text{HCN}}$ , which is consistent with the prediction that  $\text{SFE}_{\text{dense}}$  increases with  $\bar{n}$  (e.g., Riechers et al. 2007; Bussmann et al. 2008; Graciá-Carpio et al. 2008; Juneau et al. 2009; García-Burillo et al. 2012). Spatially resolved studies of the star-forming regions in local galaxies show that  $L_{\text{FIR}}/L'_{\text{HCN}}$  is strongly dependent on environment and *anticorrelated* with  $L'_{\text{HCN}}/L'_{\text{CO}}$  (e.g., Usero et al. 2015; Bigiel et al. 2016). Thus,  $L_{\text{FIR}}/L'_{\text{HCN}}$  is lower in galaxy nuclear regions, which typically show the highest  $L'_{\text{HCN}}/L'_{\text{CO}}$ , and increases in regions of low  $L'_{\text{HCN}}/L'_{\text{CO}}$ ; the overall  $L'_{\text{CO}}/L_{\text{FIR}}$  remains nearly constant. This has been interpreted as the increase in  $\text{SFE}_{\text{dense}}$  in regions of large density contrasts, instead of in regions with large dense gas fractions, which naturally leads to a lower  $\text{SFE}_{\text{dense}}$  in galaxy nuclei, despite a large  $f_{\text{dense}}$  (Bigiel et al. 2016). All these observational results are in conflict with the idea that star formation proceeds with a universal constant efficiency above a certain threshold density.

An additional source of uncertainty is the HCN to dense gas mass conversion factor  $\alpha_{\text{HCN}}$ , such that  $M_{\text{dense}} = \alpha_{\text{HCN}} L'_{\text{HCN}(J=1-0)}$ . Studies in the literature suggest that the same  $\alpha_{\text{HCN}}$  is not applicable to mergers or extreme galaxies (e.g., García-Burillo et al. 2012), and that the  $\alpha_{\text{HCN}}$  in ULIRGs needs to be lower by a factor similar to  $\alpha_{\text{CO}}$ , relative to the Milky Way (MW) canonical values. This has been taken into consideration while comparing the threshold density and turbulence-regulated star formation models (Usero et al. 2015). García-Burillo et al. (2012) also find that threshold density models place much more stringent constraints on the allowed  $\alpha_{\text{HCN}}$  and  $\alpha_{\text{CO}}$  values, as opposed to turbulence-regulated models.

### 5.3.2. Dense Molecular Gas Properties of EGS 13004291

Using our observed HCN emission and the  $L_{\text{FIR}}$  obtained from SED fitting, we calculate  $L_{\text{FIR}}/L'_{\text{HCN}}$  for EGS 13004291. Comparing our obtained value against the  $L_{\text{FIR}}/L'_{\text{HCN}}$  values for our compiled sample of galaxies (as described in Section 2.2), we find that it lies below the best-fit  $L_{\text{FIR}}-L'_{\text{HCN}}$  relation (Figure 7, middle). Thus, its  $\text{SFE}_{\text{dense}}$  (traced by  $L_{\text{FIR}}/L'_{\text{HCN}}$ ) is lower than that seen in other galaxy populations. This is inconsistent with the concept of dense gas clumps as fixed units of star formation having a constant  $\text{SFE}_{\text{dense}}$ .

EGS 13004291 has a line luminosity ratio of  $L'_{\text{HCN}}/L'_{\text{CO}} = 0.17 \pm 0.07$ , significantly higher than that seen in local spiral galaxies ( $L'_{\text{HCN}}/L'_{\text{CO}} = 0.04 \pm 0.02$ ), but consistent with that seen in local ULIRGs ( $L'_{\text{HCN}}/L'_{\text{CO}} = 0.13 \pm 0.03$ ) and high- $z$  (U) LIRGs ( $L'_{\text{HCN}}/L'_{\text{CO}} = 0.16 \pm 0.07$ ). Given that this line luminosity ratio traces the dense gas fraction  $f_{\text{dense}}$  (modulo

$\alpha_{\text{HCN}}/\alpha_{\text{CO}}$ ), this implies that the dense gas fraction in EGS 13004291 is significantly higher than that observed in normal local galaxies and is instead consistent with that displayed by some of the most extreme high- $z$  sources, including the Cloverleaf quasar and F10214+4724 (Solomon et al. 2003; Vanden Bout et al. 2004; Solomon & Vanden Bout 2005).

We can rule out the possibility that the enhanced dense gas fraction we find is caused by  $\alpha_{\text{HCN}}$  or by our assumed  $r_{21}$  to our results as follows. We have assumed  $r_{21} = 0.65$  for the HCN excitation, which is the mean value as observed in local starburst/AGN-dominated galaxies (Krips et al. 2008; Geach & Papadopoulos 2012). While no similar studies have been performed for normal local spiral galaxies, they are likely to have lower  $r_{21}$  values. The maximum values for pure starburst galaxies are  $r_{21} \lesssim 0.7$  (Krips et al. 2008), while the most extreme values have been seen upon zooming into the nuclei of galaxies with nuclear starbursts (e.g.,  $r_{21} \sim 1$  in the nuclear region of M82; Krips et al. 2008). Such extreme conditions ( $T_k \sim 40$  K, with the CO being partially optically thin; see Turner et al. 1990) are unlikely to prevail over large spatial scales in EGS 13004291, given the subthermal excitation between the  $\text{CO}(J=2 \rightarrow 1)$  and  $\text{CO}(J=3 \rightarrow 2)$  lines (Papadopoulos et al. 2012). We therefore expect that the  $r_{21}$  for EGS 13004291 is comparable to or less than  $r_{21} \sim 0.65$ . We therefore derive conservative estimates for the dense gas fraction, as lower values for  $r_{21}$  will result in a higher  $L'_{\text{HCN}(J=1-0)}$  line luminosity and a larger dense gas fraction.

Assuming a galactic  $\alpha_{\text{HCN}}^{\text{MW}} = 10M_{\odot} (\text{K km s}^{-1} \text{pc}^2)^{-1}$  (Gao & Solomon 2004b), we obtain a dense gas mass of  $M_{\text{dense}} = (1.4 \pm 0.5) \times 10^{11} M_{\odot}$ , which would imply that about half the gas mass is in the form of dense gas,  $f_{\text{dense}} \sim 0.48$ , whereas typical values for the MW and ULIRGs are typically  $\sim 3\%$  (Lada et al. 2012) and  $\sim 10\%$  (Gao et al. 2001). This suggests that  $\alpha_{\text{HCN}}$  is likely lower in EGS 13004291 than assumed here. Mechanically driven turbulence or shocks, caused by infall or outflow of large amounts of molecular gas, can also result in enhancement of HCN emission and drive down the value of  $\alpha_{\text{HCN}}$  (Imanishi & Nakanishi 2014; Martín et al. 2015).

However, if the HCN luminosity is not enhanced relative to the other dense gas tracers observed in this system, we can extend the turbulence-regulated star formation model to explain the observed properties for EGS 13004291. It is possible that the observed  $\text{SFE}_{\text{dense}}$  is low because of a turbulent and compressive (i.e., high-pressure) ISM, undergoing constant replenishment by infalling gas from the cosmic web and being rapidly consumed by star formation. An increase in  $\mathcal{M}$  results in a higher  $f_{\text{dense}}$  and a lower  $\text{SFE}_{\text{dense}}$ , which would be consistent with our observations. This fits in with the picture of a near-constant  $\text{SFE}_{\text{mol}}$  in MS galaxies and starburst galaxies lying above the MS. Silverman et al. (2015) find evidence that starburst galaxies lying above the galaxy MS show slightly higher  $\text{SFE}_{\text{CO}}$ , but by a smaller factor than in local ULIRGs and starburst galaxies. In the framework described above, the  $\text{SFE}_{\text{mol}}$  depends on  $\text{SFE}_{\text{dense}}$  and  $f_{\text{dense}}$ , which are more fundamental quantities; assuming that EGS 13004291 is not an exceptional source, this suggests that there can be naturally occurring variations in the SFE of starburst galaxies. In that case, the  $\text{SFE}_{\text{mol}}$  is not an adequate representative of star formation properties in these galaxies, and dense gas observations will be even more critical for such sources.

### 5.3.3. Other Dense Gas Tracers

We obtain a brightness temperature ratio of  $L'_{\text{HCN}}/L'_{\text{HNC}} \sim 1.8 \pm 1.3$ , and we obtain a *lower* limit of  $L'_{\text{HCN}}/L'_{\text{HCO}^+} \gtrsim 1.2$  for the  $J = 2 \rightarrow 1$  transitions. These ratios depend on multiple factors, including the relative abundance of HCN,  $\text{HCO}^+$ , and HNC and their different excitation states, given the gas density and temperature, and the gas ionization state (Aalto et al. 1994; Huettemeister et al. 1995; Lepp & Dalgarno 1996; Meijerink et al. 2007). Higher temperatures favor an increased  $\text{HCO}^+$  abundance; conversely, the HNC abundance is favored over that of HCN at lower temperatures (Schilke et al. 1992; Graninger et al. 2014), leading to the observed inverse correlation between  $L'_{\text{HCN}}/L'_{\text{HCO}^+}$  and  $L'_{\text{HCN}}/L'_{\text{HNC}}$  (e.g., Loenen et al. 2007).

Galaxies hosting AGNs typically show a higher  $L'_{\text{HCN}}/L'_{\text{HCO}^+}$  brightness temperature ratio than starburst or composite galaxies (e.g., Kohno et al. 2001; Imanishi et al. 2007; Krips et al. 2008; Izumi et al. 2015), due to a relatively enhanced HCN abundance. Privon et al. (2015) find a mean line ratio of  $L'_{\text{HCN}}/L'_{\text{HCO}^+} \sim 1.84$  for AGN hosts, while  $L'_{\text{HCN}}/L'_{\text{HCO}^+} \sim 1.14$  is found in AGN-starburst composite galaxies, and  $L'_{\text{HCN}}/L'_{\text{HCO}^+} \sim 0.88$  is found in purely starburst galaxies. However, a high  $L'_{\text{HCN}}/L'_{\text{HCO}^+}$  ratio is not uniquely associated with the presence of an AGN, as this ratio is not solely driven by relative HCN and  $\text{HCO}^+$  abundances. High  $L'_{\text{HCN}}/L'_{\text{HCO}^+}$  ratios can also be observed in UV-dominated Photon Dominated Regions (PDRs) with high densities, as well as in low-density X-ray-dominated regions (Meijerink et al. 2007; Privon et al. 2015). We assume that the  $L'_{\text{HCN}}/L'_{\text{HCO}^+}$  ratio in the  $J = 2 \rightarrow 1$  lines is representative of that in the  $J = 1 \rightarrow 0$  lines. This is a reasonable assumption for galaxies that are not AGN-dominated (see Krips et al. 2008).

Our lower limit on  $L'_{\text{HCN}}/L'_{\text{HCO}^+} \gtrsim 1.2$  is consistent with the line ratios observed in starburst galaxies (Privon et al. 2015), though it is higher than the mean line ratio ( $L'_{\text{HCN}}/L'_{\text{HCO}^+} \sim 0.88$ ). Our limit is also consistent with the observed line ratio in the Cloverleaf quasar,  $\text{HCN}/\text{HCO}^+ \sim 1.3$  (Riechers et al. 2006a), where it is proposed to arise from optically thick emission from HCN and  $\text{HCO}^+$  occupying regions of similar density and volume.

The line luminosity ratio  $L'_{\text{HCN}}/L'_{\text{HNC}}$  is a sensitive probe of the gas temperature (Graninger et al. 2014), and  $L'_{\text{HCN}}/L'_{\text{HNC}}$  has been observed to vary between  $L'_{\text{HCN}}/L'_{\text{HNC}} \sim 0.16$  and  $L'_{\text{HCN}}/L'_{\text{HNC}} \sim 2$  within a similar class of galaxies (i.e., with similar dense gas fractions traced by  $L'_{\text{HCN}}/L'_{\text{CO}}$ ; Aalto et al. 2002). We find  $L'_{\text{HCN}}/L'_{\text{HNC}} \sim 1.8 \pm 1.3$ , which is consistent but slightly higher than the canonical value for  $L'_{\text{HCN}}/L'_{\text{HNC}} \sim 1.1$  (Goldsmith et al. 1981) in the absence of a highly ionized medium. This is consistent with the expected increase in  $L'_{\text{HCN}}/L'_{\text{HNC}}$  in star-forming regions (Meier & Turner 2005). The presence of shocks or mechanically driven turbulence would also contribute to a high  $L'_{\text{HCN}}/L'_{\text{HNC}}$ , as HNC is preferentially destroyed in shocks (Schilke et al. 1992; Lindberg et al. 2016).

### 5.3.4. Sources of Uncertainty

We note our results are subject to the uncertainties inherent to the use of  $L_{\text{FIR}}$  as a tracer for star formation. While a

significant fraction of the star formation in nearby spirals and high- $z$  disk galaxies is not dust-obscured (see Section 5.2), sources such as nearby ULIRGs, high- $z$  SMGs, and FIR-luminous quasars are typically dominated by dust-obscured star formation. Thus, the  $L_{\text{FIR}}$  is a reasonable estimator for the SFR in our archival sample of high- $z$  sources, all of which belong to the latter category. However, only 30% of the star formation activity in EGS 13004291 is dust-obscured. We investigate the impact of this finding on our study by defining an “equivalent” FIR luminosity  $L_{\text{FIR}}^{\text{eq}}$ , such that the total SFR obtained from our SED fitting (including both UV and FIR emission) corresponds to  $\text{SFR}_{\text{UV+FIR}} = 1.07 \times 10^{-10} L_{\text{FIR}}^{\text{eq}}$ . The alternative constraints obtained using this value are shown as gray crosses in Figure 7 for comparison. We find that adopting  $L_{\text{FIR}}^{\text{eq}}$  would not significantly affect our overall results.

### 5.4. Comparison with Other MS Galaxies

A number of studies have focused on the bimodality of star formation modes in high- $z$  galaxies, with the bulk proceeding quiescently and a small population of starbursts having higher star formation efficiencies and correspondingly shorter gas depletion timescales (e.g., Daddi et al. 2010b; Rodighiero et al. 2011). However, recent work on large samples of MS galaxies and on outliers above the MS may suggest that all SFGs have the same gas depletion timescale  $\tau_{\text{depl}}$  and therefore the same star formation efficiency (e.g., Scoville et al. 2015). These authors argue that this short, constant depletion time for both MS and above-MS galaxies is due to a different mode of SF prevailing at high redshifts, driven by either compressive and rapid gas motions or galaxy–galaxy mergers, with the dispersive gas motion arising from the rapid accretion needed to maintain the high SFR. This would be a more efficient mode for star formation from existing gas supplies at high redshift, applying to both MS and above-MS galaxies.

EGS 13004291 lies above the MS, with an  $\text{sSFR}/\text{sSFR}_{\text{MS}} \sim 13$ . Despite being a starburst, we find that its SFE is not enhanced relative to other MS galaxies; it is consistent within the scatter (see Figure 6(a) by Dessauges-Zavadsky et al. 2015). This fits in with the model described above, where both MS and above-MS galaxies have the same gas depletion timescale. The lack of enhancement in the  $\text{SFE}_{\text{mol}}$  is also consistent with turbulence-regulated star formation models, since the relative effects of an enhanced  $f_{\text{dense}}$  and a lower  $\text{SFE}_{\text{dense}}$  cancel each other out. Given that our  $\text{SFE}_{\text{mol}}$  is consistent with that found in MS galaxies at the same epoch, our higher dense gas fraction also fits in with a star formation mode where the ISM is compressive and more turbulent; star formation would no longer proceed in isolated dense gas clumps as in the Milky Way, but in a more widespread manner throughout the disk, so the idea of dense gas clumps as discrete units of star formation would no longer be applicable. This is similar to the prevalent picture in ULIRGs (Solomon & Vanden Bout 2005), although in a milder form because it is driven by less extreme processes than merging galaxies.

## 6. Conclusions

We have tentatively detected dense molecular gas, using HCN and HNC as tracers, and constrained the CO excitation in

EGS 13004291, one of the most gas-rich star-forming galaxies detected at high redshift. We find the following:

1. The CO excitation in EGS 13004291 is subthermal and consistent with that seen in BzK galaxies and significantly different from IR-luminous sources such as the Cloverleaf quasar and F10214+4724, which show nearly thermalized CO emission up to  $J = 4$ .
2. The SFE in EGS 13004291 is consistent with literature values for the galaxy MS at  $z \sim 1$ , unlike starbursts in the local universe, which show higher SFEs as compared to normal galaxies.
3. The dense gas fraction  $f_{\text{dense}}$  for EGS 13004291, as traced by  $L'_{\text{HCN}}/L'_{\text{CO}} = 0.17 \pm 0.07$ , is significantly enhanced over that in normal spiral galaxies at  $z \sim 0$  but is instead consistent with the values typically displayed by ULIRGs and those found for SMGs at high redshift.
4. Additionally, we report the serendipitous detection of CO rotational transitions in two high- $z$  sources in our HCN observations, one of which, if confirmed, would be the highest-redshift MS galaxy detected in CO to date.

Overall, we find that the SFE for the starburst EGS 13004291 is consistent with that for normal MS galaxies at high redshift, which is in sharp contrast to the difference found between normal and starburst galaxy populations in the local universe. Together with the enhanced dense gas fraction observed in EGS 13004291, this indicates that the rapid star formation in high- $z$  starburst galaxies does not proceed analogously to that in local starburst galaxies. More critically, this difference cannot be quantified by using only  $L_{\text{FIR}}/L'_{\text{CO}}$  as a proxy for the SFE. Our observations support the model of a constant depletion timescale in both MS and starburst galaxies resulting from a turbulent, compressive ISM; the logical next step is to perform such studies for a larger sample of MS and starburst galaxies at high redshift. Observations of the dense gas component will be vital, as studies of the  $L_{\text{FIR}}/L'_{\text{CO}}$  alone will miss variations in the SFE<sub>dense</sub> and  $f_{\text{dense}}$ . Such observations are now feasible with both ALMA and NOEMA, and will demonstrate whether enhanced dense gas fractions are universally found in MS and starburst galaxies, or whether EGS 13004291 is an outlier, with an enhanced dense gas fraction resulting from an infall or outflow of molecular gas. Concurrent observations of other dense gas tracers are also important, to confirm the utility of HCN as a dense gas tracer, and are well within the reach of ALMA and NOEMA's wide-bandwidth receivers. Finally, spatially resolved studies of dense gas star formation in the local universe, such as the ongoing EMPIRE survey (Bigiel et al. 2016), will help to clarify the role of turbulence-regulated or density threshold models in star formation.

We would like to thank the anonymous referee for highly detailed and constructive comments that improved the clarity of our results. We thank Denis Burgarella for his invaluable assistance with the CIGALE SED-fitting code and Gordon Stacey for enlightening comments on the CO-to-H<sub>2</sub> conversion factor. This research has made use of NASA's Astrophysics Data System. D.R. and R.P. acknowledge support from the National Science Foundation under grant number AST-1614213 to Cornell University. R.P. acknowledges support through award SOSPA3-008 from the NRAO. H.D. acknowledges financial support from the Spanish Ministry of Economy

and Competitiveness (MINECO) under the 2014 Ramón y Cajal program MINECO RYC-2014-15686. This study makes use of data from AEGIS, a multiwavelength sky survey conducted with the *Chandra*, *GALEX*, Hubble, Keck, CFHT, MMT, Subaru, Palomar, *Spitzer*, VLA, and other telescopes and was supported in part by the NSF, NASA, and the STFC. This work is based on observations taken by the 3D-HST Treasury Program (HST-GO-12177 and HST-GO-12328) with the NASA/ESA *Hubble Space Telescope*, which is operated by the Association of Universities for Research in Astronomy, Inc., under NASA contract NAS5-26555. This study makes use of data from the NEWFIRM Medium-band Survey, a multi-wavelength survey conducted with the NEWFIRM instrument at the KPNO, supported in part by the NSF and NASA.

## References

- Aalto, S., Booth, R. S., Black, J. H., Koribalski, B., & Wielebinski, R. 1994, *A&A*, **286**, 365
- Aalto, S., Polatidis, A. G., Hüttemeister, S., & Curran, S. J. 2002, *A&A*, **381**, 783
- Aniano, G., Draine, B. T., Calzetti, D., et al. 2012, *ApJ*, **756**, 138
- Aravena, M., Hodge, J. A., Wagg, J., et al. 2014, *MNRAS*, **442**, 558
- Barmby, P., Huang, J.-S., Ashby, M. L. N., et al. 2008, *ApJS*, **177**, 431
- Bigiel, F., Leroy, A. K., Jiménez-Donaire, M. J., et al. 2016, *ApJL*, **822**, L26
- Binney, J., & Tremaine, S. 2008, *Galactic Dynamics* (2nd ed.; Princeton, NJ: Princeton Univ. Press)
- Blain, A. W., Smail, I., Ivison, R. J., Kneib, J.-P., & Frayer, D. T. 2002, *PhR*, **369**, 111
- Bolatto, A. D., Wolfire, M., & Leroy, A. K. 2013, *ARA&A*, **51**, 207
- Bothwell, M. S., Chapman, S. C., Tacconi, L., et al. 2010, *MNRAS*, **405**, 219
- Bothwell, M. S., Smail, I., Chapman, S. C., et al. 2013, *MNRAS*, **429**, 3047
- Bouché, N., Dekel, A., Genzel, R., et al. 2010, *ApJ*, **718**, 1001
- Bournaud, F., Daddi, E., Weiß, A., et al. 2015, *A&A*, **575**, A56
- Brammer, G. B., van Dokkum, P. G., & Coppi, P. 2008, *ApJ*, **686**, 1503
- Brammer, G. B., van Dokkum, P. G., Franx, M., et al. 2012, *ApJS*, **200**, 13
- Bruzual, G., & Charlot, S. 2003, *MNRAS*, **344**, 1000
- Bussmann, R. S., Narayanan, D., Shirley, Y. L., et al. 2008, *ApJL*, **681**, L73
- Calzetti, D., Armus, L., Bohlin, R. C., et al. 2000, *ApJ*, **533**, 682
- Carilli, C. L., Solomon, P., Vanden Bout, P., et al. 2005, *ApJ*, **618**, 586
- Carilli, C. L., & Walter, F. 2013, *ARA&A*, **51**, 105
- Carleton, T., Cooper, M. C., Bolatto, A. D., et al. 2016, arXiv:1611.04587
- Casey, C. M. 2012, *MNRAS*, **425**, 3094
- Casey, C. M., Narayanan, D., & Cooray, A. 2014, *PhR*, **541**, 45
- Charlot, S., & Fall, S. M. 2000, *ApJ*, **539**, 718
- Costagliola, F., Aalto, S., Rodríguez, M. I., et al. 2011, *A&A*, **528**, A30
- da Cunha, E., Charlot, S., & Elbaz, D. 2008, *MNRAS*, **388**, 1595
- da Cunha, E., Walter, F., Smail, I. R., et al. 2015, *ApJ*, **806**, 110
- Daddi, E., Bournaud, F., Walter, F., et al. 2010a, *ApJ*, **713**, 686
- Daddi, E., Dannerbauer, H., Elbaz, D., et al. 2008, *ApJL*, **673**, L21
- Daddi, E., Dannerbauer, H., Liu, D., et al. 2015, *A&A*, **577**, A46
- Daddi, E., Dickinson, M., Morrison, G., et al. 2007, *ApJ*, **670**, 156
- Daddi, E., Elbaz, D., Walter, F., et al. 2010b, *ApJL*, **714**, L118
- Dale, D. A., Helou, G., Magdis, G. E., et al. 2014, *ApJ*, **784**, 83
- Danielson, A. L. R., Swinbank, A. M., Smail, I., et al. 2011, *MNRAS*, **410**, 1687
- Dannerbauer, H., Daddi, E., Riechers, D. A., et al. 2009, *ApJL*, **698**, L178
- Davis, M., Guhathakurta, P., Konidaris, N. P., et al. 2007, *ApJL*, **660**, L1
- Dessauges-Zavadsky, M., Zamojski, M., Schaerer, D., et al. 2015, *A&A*, **577**, A50
- Downes, D., & Solomon, P. M. 1998, *ApJ*, **507**, 615
- Draine, B. T., & Li, A. 2007, *ApJ*, **657**, 810
- Elbaz, D., Daddi, E., Le Borgne, D., et al. 2007, *A&A*, **468**, 33
- Engel, H., Tacconi, L. J., Davies, R. I., et al. 2010, *ApJ*, **724**, 233
- Evans, A. S., Solomon, P. M., Tacconi, L. J., Vavilkin, T., & Downes, D. 2006, *AJ*, **132**, 2398
- Freundlich, J., Combes, F., Tacconi, L. J., et al. 2013, *A&A*, **553**, A130
- Fritz, J., Franceschini, A., & Hatziminaoglou, E. 2006, *MNRAS*, **366**, 767
- Gao, Y., Carilli, C. L., Solomon, P. M., & Vanden Bout, P. A. 2007, *ApJL*, **660**, L93
- Gao, Y., Lo, K. Y., Lee, S.-W., & Lee, T.-H. 2001, *ApJ*, **548**, 172
- Gao, Y., & Solomon, P. M. 2004a, *ApJS*, **152**, 63
- Gao, Y., & Solomon, P. M. 2004b, *ApJ*, **606**, 271

- García-Burillo, S., Usero, A., Alonso-Herrero, A., et al. 2012, *A&A*, **539**, A8
- Geach, J. E., & Papadopoulos, P. P. 2012, *ApJ*, **757**, 156
- Genzel, R., Tacconi, L. J., Gracia-Carpio, J., et al. 2010, *MNRAS*, **407**, 2091
- Genzel, R., Tacconi, L. J., Lutz, D., et al. 2015, *ApJ*, **800**, 20
- Goldsmith, P. F., Langer, W. D., Ellender, J., Kollberg, E., & Irvine, W. 1981, *ApJ*, **249**, 524
- Graciá-Carpio, J., García-Burillo, S., Planesas, P., & Colina, L. 2006, *ApJL*, **640**, L135
- Graciá-Carpio, J., García-Burillo, S., Planesas, P., Fuente, A., & Usero, A. 2008, *A&A*, **479**, 703
- Graninger, D. M., Herbst, E., Öberg, K. I., & Vasyunin, A. I. 2014, *ApJ*, **787**, 74
- Greve, T. R., Bertoldi, F., Smail, I., et al. 2005, *MNRAS*, **359**, 1165
- Greve, T. R., Hainline, L. J., Blain, A. W., et al. 2006, *AJ*, **132**, 1938
- Groves, B. A., Schinnerer, E., Leroy, A., et al. 2015, *ApJ*, **799**, 96
- Hodge, J. A., Carilli, C. L., Walter, F., et al. 2012, *ApJ*, **760**, 11
- Huang, J.-S., Faber, S. M., Daddi, E., et al. 2009, *ApJ*, **700**, 183
- Huettemeister, S., Henkel, C., Mauersberger, R., et al. 1995, *A&A*, **295**, 571
- Imanishi, M., & Nakanishi, K. 2014, *AJ*, **148**, 9
- Imanishi, M., Nakanishi, K., Tamura, Y., Oi, N., & Kohno, K. 2007, *AJ*, **134**, 2366
- Isaak, K. G., Chandler, C. J., & Carilli, C. L. 2004, *MNRAS*, **348**, 1035
- Iverson, R. J., Papadopoulos, P. P., Smail, I., et al. 2011, *MNRAS*, **412**, 1913
- Izumi, T., Kohno, K., Aalto, S., et al. 2015, *ApJ*, **811**, 39
- Izumi, T., Kohno, K., Aalto, S., et al. 2016, *ApJ*, **818**, 42
- Juneau, S., Narayanan, D. T., Moustakas, J., et al. 2009, *ApJ*, **707**, 1217
- Karim, A., Schinnerer, E., Martínez-Sansigre, A., et al. 2011, *ApJ*, **730**, 61
- Kennicutt, R. C., Jr. 1998, *ApJ*, **498**, 541
- Kewley, L. J., Geller, M. J., Jansen, R. A., & Dopita, M. A. 2002, *AJ*, **124**, 3135
- Kohno, K., Matsushita, S., Vila-Vilaró, B., et al. 2001, in ASP Conf. Ser. 249, The Central Kiloparsec of Starbursts and AGN: The La Palma Connection, ed. J. H. Knapen et al. (San Francisco, CA: ASP), 672
- Krips, M., Crocker, A. F., Bureau, M., Combes, F., & Young, L. M. 2010, *MNRAS*, **407**, 2261
- Krips, M., Neri, R., García-Burillo, S., et al. 2008, *ApJ*, **677**, 262
- Krumholz, M. R., & McKee, C. F. 2005, *ApJ*, **630**, 250
- Krumholz, M. R., & Thompson, T. A. 2007, *ApJ*, **669**, 289
- Lada, C. J., Forbrich, J., Lombardi, M., & Alves, J. F. 2012, *ApJ*, **745**, 190
- Laird, E. S., Nandra, K., Georgakakis, A., et al. 2009, *ApJS*, **180**, 102
- Lee, N., Sanders, D. B., Casey, C. M., et al. 2015, *ApJ*, **801**, 80
- Lepp, S., & Dalgarno, A. 1996, *A&A*, **306**, L21
- Leroy, A. K., Bolatto, A., Gordon, K., et al. 2011, *ApJ*, **737**, 12
- Lilly, S. J., Carollo, C. M., Pipino, A., Renzini, A., & Peng, Y. 2013, *ApJ*, **772**, 119
- Lindberg, J. E., Aalto, S., Muller, S., et al. 2016, *A&A*, **587**, A15
- Loenen, A. F., Baan, W. A., & Spaans, M. 2007, in IAU Symp. 242, Astrophysical Masers and their Environments, ed. J. M. Chapman & W. A. Baan, 462
- Magdis, G. E., Daddi, E., Elbaz, D., et al. 2011, *ApJL*, **740**, L15
- Maraston, C. 2005, *MNRAS*, **362**, 799
- Martín, S., Kohno, K., Izumi, T., et al. 2015, *A&A*, **573**, A116
- Meier, D. S., & Turner, J. L. 2005, *ApJ*, **618**, 259
- Meijerink, R., Spaans, M., & Israel, F. P. 2007, *A&A*, **461**, 793
- Nandra, K., Laird, E. S., Aird, J. A., et al. 2015, *ApJS*, **220**, 10
- Noeske, K. G., Faber, S. M., Weiner, B. J., et al. 2007, *ApJL*, **660**, L47
- Noll, S., Burgarella, D., Giovannoli, E., et al. 2009, *A&A*, **507**, 1793
- Papadopoulos, P. P. 2007, *ApJ*, **656**, 792
- Papadopoulos, P. P., van der Werf, P. P., Xilouris, E. M., et al. 2012, *MNRAS*, **426**, 2601
- Pettini, M., Shapley, A. E., Steidel, C. C., et al. 2001, *ApJ*, **554**, 981
- Privon, G. C., Herrero-Illana, R., Evans, A. S., et al. 2015, *ApJ*, **814**, 39
- Rémy-Ruyer, A., Madden, S. C., Galliano, F., et al. 2014, *A&A*, **563**, A31
- Riechers, D. A., Bradford, C. M., Clements, D. L., et al. 2013, *Natur*, **496**, 329
- Riechers, D. A., Carilli, C. L., Capak, P. L., et al. 2014, *ApJ*, **796**, 84
- Riechers, D. A., Carilli, C. L., Maddalena, R. J., et al. 2011a, *ApJL*, **739**, L32
- Riechers, D. A., Carilli, C. L., Walter, F., & Momjian, E. 2010a, *ApJL*, **724**, L153
- Riechers, D. A., Hodge, J., Walter, F., Carilli, C. L., & Bertoldi, F. 2011b, *ApJL*, **739**, L31
- Riechers, D. A., Walter, F., Bertoldi, F., et al. 2009a, *ApJ*, **703**, 1338
- Riechers, D. A., Walter, F., Carilli, C. L., et al. 2006a, *ApJL*, **645**, L13
- Riechers, D. A., Walter, F., Carilli, C. L., et al. 2006b, *ApJ*, **650**, 604
- Riechers, D. A., Walter, F., Carilli, C. L., & Bertoldi, F. 2007, *ApJL*, **671**, L13
- Riechers, D. A., Walter, F., Carilli, C. L., & Lewis, G. F. 2009b, *ApJ*, **690**, 463
- Riechers, D. A., Weiß, A., Walter, F., & Wagg, J. 2010b, *ApJ*, **725**, 1032
- Rodighiero, G., Daddi, E., Baronchelli, I., et al. 2011, *ApJL*, **739**, L40
- Sanders, D. B., & Mirabel, I. F. 1996, *ARA&A*, **34**, 749
- Sandstrom, K. M., Leroy, A. K., Walter, F., et al. 2013, *ApJ*, **777**, 5
- Santini, P., Maiolino, R., Magnelli, B., et al. 2010, *A&A*, **518**, L154
- Schilke, P., Walmsley, C. M., Pineau Des Forets, G., et al. 1992, *A&A*, **256**, 595
- Schmidt, M. 1959, *ApJ*, **129**, 243
- Scoville, N., Sheth, K., Aussel, H., et al. 2015, arXiv:1505.02159
- Seko, A., Ohta, K., Yabe, K., et al. 2016, *ApJ*, **819**, 82
- Serra, P., Amblard, A., Temi, P., et al. 2011, *ApJ*, **740**, 22
- Sharon, C. E., Riechers, D. A., Hodge, J., et al. 2016, arXiv:1606.02309
- Silverman, J. D., Daddi, E., Rodighiero, G., et al. 2015, *ApJL*, **812**, L23
- Skelton, R. E., Whitaker, K. E., Momcheva, I. G., et al. 2014, *ApJS*, **214**, 24
- Solomon, P., Vanden Bout, P., Carilli, C., & Guélin, M. 2003, *Natur*, **426**, 636
- Solomon, P. M., Downes, D., Radford, S. J. E., & Barrett, J. W. 1997, *ApJ*, **478**, 144
- Solomon, P. M., & Vanden Bout, P. A. 2005, *ARA&A*, **43**, 677
- Speagle, J. S., Steinhardt, C. L., Capak, P. L., & Silverman, J. D. 2014, *ApJS*, **214**, 15
- Spergel, D. N., Bean, R., Doré, O., et al. 2007, *ApJS*, **170**, 377
- Swinbank, A. M., Simpson, J. M., Smail, I., et al. 2014, *MNRAS*, **438**, 1267
- Symeonidis, M., Georgakakis, A., Page, M. J., et al. 2014, *MNRAS*, **443**, 3728
- Symeonidis, M., Georgakakis, A., Seymour, N., et al. 2011, *MNRAS*, **417**, 2239
- Tacconi, L. J., Genzel, R., Neri, R., et al. 2010, *Natur*, **463**, 781
- Tacconi, L. J., Neri, R., Genzel, R., et al. 2013, *ApJ*, **768**, 74
- Thomson, A. P., Iverson, R. J., Smail, I., et al. 2012, *MNRAS*, **425**, 2203
- Turner, J. L., Martin, R. N., & Ho, P. T. P. 1990, *ApJ*, **351**, 418
- Usero, A., Leroy, A. K., Walter, F., et al. 2015, *AJ*, **150**, 115
- Vanden Bout, P. A., Solomon, P. M., & Maddalena, R. J. 2004, *ApJL*, **614**, L97
- Wagg, J., Wilner, D. J., Neri, R., Downes, D., & Wiklind, T. 2005, *ApJL*, **634**, L13
- Weiß, A., Downes, D., Neri, R., et al. 2007, *A&A*, **467**, 955
- Weiß, A., Henkel, C., Downes, D., & Walter, F. 2003, *A&A*, **409**, L41
- Whitaker, K. E., Labbé, I., van Dokkum, P. G., et al. 2011, *ApJ*, **735**, 86
- Whitaker, K. E., van Dokkum, P. G., Brammer, G., & Franx, M. 2012, *ApJL*, **754**, L29
- Wu, J., Evans, N. J., II, Gao, Y., et al. 2005, *ApJL*, **635**, L173
- Wu, J., Evans, N. J., II, Shirley, Y. L., & Knez, C. 2010, *ApJS*, **188**, 313
- Wuyts, S., Förster Schreiber, N. M., Lutz, D., et al. 2011, *ApJ*, **738**, 106
- Zavala, J. A., Yun, M. S., Aretxaga, I., et al. 2015, *MNRAS*, **452**, 1140